Université de Montréal

Mesure de haute résolution de la fonction de distribution radiale du silicium amorphe pur

par
Khalid Laaziri
Département de physique
Faculté des arts et des sciences

Thèse présentée à la Faculté des études supérieures
en vue de l'obtention du grade de
Philosophiæ Doctor (Ph. D.)
en physique

Mai, 1999

Université de Montréal

Mesure de haute résolution de la fonction de distribution radiale du silicium amorphe pur

par

Khalid Laaziri

Département de physique

Faculté des arts et des sciences

Thèse présentée à la Faculté des études supérieures
en vue de l'obtention du grade de
Philosophiæ Doctor (Ph.D.)
en physique

Université de Montréal

Faculté des études supérieures

Cette thèse intitulée:

Mesure de haute résolution de la fonction de distribution radiale du silicium amorphe pur

présentée par:

Khalid Laaziri

a été évaluée par un jury composé des personnes suivantes:

Laurent J. Lewis   président-rapporteur

Sjoerd Roorda   directeur de recherche

Robert W. Cochrane   membre du jury

Simon J. L. Billinge   examinateur externe

Thèse acceptée le: 6 mai 1999

À mes très chers parents et à mes frères Taoufik, Yassir et Younes ainsi que tata,

qu'ils trouvent dans cette dédicace l'expression d'une reconnaissance éternelle.

À ma très chère et adorable épouse Habiba,

qui a su de par sa gentillesse et sa patience me soutenir dans les moments difficiles,

Merci du fond du cœur, cette thèse est la tienne.

Au petit Ayman dont j'attends l'arrivée avec impatience (in chaa Allah).

À toutes les personnes qui me sont très chères,

SOMMAIRE

Cette thèse porte sur l'étude de la structure du silicium amorphe préparé par irradiation ionique. Elle présente des mesures de diffraction de rayons X sur de la poudre de silicium cristallin, du silicium amorphe relaxé et non relaxé, ainsi que tous les développements mathématiques et physiques nécessaires pour extraire la fonction de distribution radiale correspondant à chaque échantillon.

Au Chapitre I, nous présentons une méthode de fabrication de membranes minces (une dizaine de microns d'épaisseur) de silicium amorphe pur. Il y a deux étapes majeures lors du processus de fabrication: l'implantation ionique, afin de créer une couche amorphe de plusieurs microns et l'attaque chimique, pour enlever le reste du matériau cristallin. L'article présente tout d'abord une description détaillée du processus d'implantation ionique et de l'attaque chimique. Nous avons caractérisé premièrement les membranes de silicium amorphe par spectroscopie Raman pour vérifier qu'il ne reste plus de trace de matériau cristallin dans les films amorphes. Une deuxième caractérisation par détection de recul élastique (ERD-TOF) sur ces mêmes membranes a montré qu'il y a moins de 0.1% atomique de contaminants tels que l'oxygène, le carbone, et l'hydrogène.

Au Chapitre II, nous proposons une approche novatrice dans le domaine de l'analyse des spectres en énergie de diffusion de rayons X par la matière, plus

précisément une nouvelle méthode de correction de la contribution inélastique "*Compton*" des spectres de diffusion totale afin d'extraire les pics de diffusion élastique, responsable de la diffraction de Bragg. L'article présente tout d'abord une description simplifiée d'une théorie sur la diffusion inélastique dite « Impulse Approximation » (IA) qui permet de calculer des profils de Compton en fonction de l'énergie et de l'angle de diffusion 2θ. Ces profils sont utilisés comme fonction de lissage de la diffusion Compton expérimentale. Pour lisser les pics de diffusion élastique, nous avons utilisé une fonction pic de nature asymétrique. La procédure de lissage des spectres en énergie est décrite en détail, ainsi que le programme informatique permettant de générer les profils Compton. Les résultats obtenus par cette procédure sont présentés pour une gamme de spectres en énergie pris pour différents angles de diffusion 2θ.

Aux Chapitre III, nous exposons de manière détaillée les résultats des expériences de diffraction de rayons X sur les membranes de silicium amorphe et la poudre de silicium cristallin que nous avons préparées. Nous abordons aussi les différentes étapes expérimentales, d'analyse ainsi que les méthodes de détermination et de filtrage des transformées de Fourier des données de diffraction. Une comparaison des fonctions de distribution radiale du silicium amorphe relaxé et non relaxé, mesurées à haute précision, indique que la relaxation structurelle dans le silicium amorphe est probablement due en grande partie à une annihilation des défauts plutôt qu'à une réorganisation atomique globale du réseau de silicium

amorphe. La déduction de la coordination des pics correspondants au premiers voisins atomiques par lissage de fonctions gaussienne indique que la coordination du silicium amorphe relaxé est de 3.88, celle du non-relaxé est de 3.79, alors que la mesure de référence sur la poudre de silicium cristallin donne une valeur de 4 tel que prévu. La sous-coordination du silicium amorphe expliquerait pourquoi sa densité est inférieure à celle du silicium cristallin. Nous verrons aussi que la variation de la coordination en fonction de Q_{max} (borne supérieure de la gamme de l'espace réciproque sondé) indique que pour mesurer une fonction de distribution radiale fiable et précise du silicium amorphe, il faut entreprendre un balayage à au moins 40 Å⁻¹ dans l'espace réciproque.

TABLE DES MATIÈRES

INTRODUCTION

Durant les dernières décennies, les matériaux amorphes ont eu un impact formidable dans le domaine de la science et de la technologie. En effet, leurs applications couvrent plusieurs champs d'intérêt tels que les télécommunications (fibres optiques, guides d'ondes, etc), l'énergie solaire (cellules photovoltaïques), etc. Mais il reste que beaucoup des propriétés fondamentales de ces solides ne sont pas encore comprises. En effet, la structure atomique, qui est une donnée essentielle pour une compréhension détaillée des propriétés physiques et chimiques de ces solides amorphes, n'est pas encore connue de manière précise et satisfaisante.

Les matériaux amorphes se caractérisent, d'un point de vue structural, par l'absence de périodicité des arrangements atomiques. Ils ne possèdent pas de symétrie et ne présentent pas d'ordre à longue distance. On imagine aisément que la caractérisation d'une telle structure atomique sera un problème d'une extrême complexité. C'est pour cette raison que la modélisation joue un rôle très important dans l'étude de ces matériaux. Elle permet, entre autre, de répondre à certaines questions importantes. Par exemple, quel est l'arrangement local des atomes dans un matériau donné? À plus grande échelle, les assemblages d'un plus grand nombre d'atomes possèdent-ils, au-delà de leur variabilité, des caractéristiques communes?

1- Fonction de distribution radiale :

L'une des représentations les plus caractéristiques de la structure amorphe est la fonction de distribution radiale, qui est une représentation spatiale unidimensionnelle de la structure atomique. La RDF est le véritable outil qui permet de comparer la modélisation avec l'expérience. De manière expérimentale, la RDF est accessible grâce à une transformée de Fourier des intensités de diffraction obtenues soit par rayons X, neutrons ou électrons [1-3]. En effet, supposons que deux atomes, repérés par i et j, soient distants de r_{ij}. Par suite du désordre, il existe, dans toute direction, deux autres atomes k et l, également séparés par cette même distance, $r_{ij} = r_{kl}$. Il en résulte que l'intensité diffusée ne change pas avec la direction et dépend seulement de la grandeur du vecteur d'onde de diffusion Q. Dans une expérience de diffusion élastique classique, on mesure l'intensité de la diffusion d'un faisceau de rayons X monochromatique de longueur d'onde, λ, en fonction de l'angle de diffusion 2θ, qui est relié au module du vecteur d'onde par $Q = 4\pi\lambda^{-1}\sin\theta$. L'intensité cohérente diffusée est $I_{eu} = N f^2$, où f est le facteur de diffusion atomique. Si le milieu est considéré en première approximation comme un ensemble de N atomes identiques diffusant indépendamment, l'interférence des ondes émises par chaque atome conduit à des modulations autour d'une valeur moyenne $<f^2>$: ce sont ces modulations, représentées par le facteur de structure S(Q), qui contiennent les informations structurales

$$S(Q) = 1 + \frac{1}{N} \sum_{m=1}^{N} \sum_{n \neq m} \frac{\sin Q r_{mn}}{Q r_{mn}} \qquad (1)$$

Chaque distance r_{mn} dans l'échantillon est caractérisée dans $S(Q)$ par une onde sinusoïdale de période $\Delta Q = 2\pi/r_{mn}$.

La méthode ci-dessus est d'une grande clarté pédagogique, mais d'un emploi direct plutôt lourd. En pratique, on considère le milieu comme un ensemble d'atomes caractérisé par une concentration locale $\rho(r)$ au point r. À partir d'un atome donné (une valeur de m dans la première sommation de (1)), la deuxième sommation peut être transformée en une intégration sur la distance r à cet atome. Le nombre d'atomes dans une coquille sphérique de rayon r et d'épaisseur dr est

$$J(r) = 4\pi r^2 \rho(r) = rG(r) + 4\pi r^2 \rho_o \qquad (2)$$

$J(r)$ est la fonction de distribution radiale et $G(r)$ est la fonction de distribution de radiale réduite, probabilité de trouver un atome à la distance r d'un autre. Puisqu'il existe nécessairement un atome au centre de la coquille, l'intensité diffusée est proportionnelle non pas au nombre d'atomes, mais à son écart à la valeur moyenne, $4\pi r^2[\rho(r)-\rho_o]$, où ρ_o est la densité moyenne. La première sommation revient à faire la même intégrale N fois (à partir de chaque atome m). Il vient alors :

$$S(Q) = 1 + \frac{1}{Q}\int_0^\infty 4\pi r[\rho(r) - \rho_o]\sin Qr\,dr = 1 + \frac{1}{Q}\int_0^\infty G(r)\sin Qr\,dr \qquad (3)$$

On voit ainsi que la transformée de Fourier du facteur de structure permet d'accéder à l'information structurale via la fonction $G(r)$.

La fonction de distribution radiale est donc l'outil primordiale pour sonder la structure des matériaux amorphes. Malgré le fait que cette fonction n'est qu'une représentation uni-dimensionnelle de la structure, elle permet d'obtenir des

informations pertinentes tel que la coordination atomique et la position entre proches voisins ainsi que les paramètres du désordre (largeurs des pics) déterminés à partir de lissage des différents pics contenu dans la RDF. Par la suite, l'approche principale pour l'interprétation des fonctions de distribution radiale passe par la modélisation, que se soit manuelle ou générée par ordinateur.

2- Modèle aléatoire continue :

Historiquement, la premier modèle décrivant la structure des solides amorphes covalents a été décrit par Zachariasen [4] pour les verres à base de silice. En effet, en 1932, Zachariasen a émis l'hypothèse que les atomes d'un solide amorphe se répartissent sous la forme d'un réseau continu tri-dimensionnel semblable au réseau cristallin. Pourtant, à la différence du réseau cristallin, ce réseau est irrégulier: chacune de ces mailles est un peu déformée. En accumulant progressivement les perturbations aléatoires des longueurs de liaisons et des angles entre elles aménent la disparition de l'ordre à longue distance. Au début des années 70, l'apparition du silicium amorphe (a-Si) comme matériaux dans l'industrie de la micro-électronique a poussé les chercheurs à essayer de mieux comprendre ce nouveau matériau. De part sa constitution comme matériau covalent monoatomique, dont la base unitaire est l'atome de Si, le silicium amorphe est le modèle type pour l'étude de la structure amorphe. De plus, il présente un défi très intéressant pour les scientifiques puisque les premières mesures expérimentales de sa RDF [5] où on observe l'apparition du premier et deuxième pic similaire à la structure cristalline mais plus large, alors que le troisième pic qui est prédominant dans le silicium cristallin (c-Si) en est absent, les

autres pics plus éloignés se chevauchent et deviennent très large. La structure du silicium amorphe a été décrite la première fois par le modèle de réseau aléatoire continu (CRN)[1] [6] qui est, en faite, une extension du modèle de Zachariasen. La caractéristique principale de cette structure, construite manuellement à partir de boules sphériques et de bâtons en plastique, réside dans l'existence d'un ordre chimique à courte portée (conservation de la structure tétraèdrique de l'atome de silicium ainsi que sa coordination de 4), et l'absence d'ordre à grande portée (périodicité); ce modèle a été étendue à un plus grand nombre d'atomes par Polk et Boudreaux [7]. Les premiers modèles générés par ordinateur ont fait leurs apparitions par la suite [8,9] et avec le développement d'ordinateurs et des techniques de simulations (dynamique moléculaire et monte-carlo), une multitude de modèles plus réalistes décrivant la structure du silicium amorphe a été calculée [10-15]. Les principaux résultats de ces travaux indiquent que la nature tétraèdrique de la structure cristalline est conservée dans le réseau amorphe et la coordination atomique des proches voisins est de 4 et parfois plus. Mais, il reste que la validité de ces modèles doit être testée avec les résultats des différentes expériences caractérisant la structure atomique, plus particulièrement la fonction de distribution radiale (RDF)[2] obtenue à partir de mesure de diffraction. En effet, l'apport principal d'une RDF expérimentale précise serait de donner l'outil nécessaire permettant de faire la distinction entre les multiples modèles générés par les différentes technique de simulation, et ainsi vérifier l'authenticité du CRN. Il reste que malgré les efforts répétés des chercheurs, la

---

[1] *Continuous Random Network*
[2] *Radial Distribution Function*

fonction de distribution radiale du silicium amorphe n'est pas encore fiable et connue de manière précise [5,16-24]. Par exemple, la coordination atomique des premiers voisins n'est pas encore connue de manière précise.

3- Fiabilité de la fonction de distribution radiale :

Il y deux raisons essentielles qui peuvent expliquer pourquoi les mesures de la RDF du silicium amorphe ne sont pas fiables. Premièrement, la majorité des échantillons de silicium ou de germanium amorphe utilisés dans le cadre de ces expériences de diffraction sont produits par des techniques de dépôts telles que l'évaporation sous vide ou la pulvérisation. Ces méthodes de dépôt ont le désavantage de produire des matériaux amorphes présentant des hétérogénéités structurelles macroscopiques (cavité de vide), ainsi que l'introduction d'impuretés à différents degrés de concentration [5,25]. Ceci aura pour résultat de fausser les données de la RDF, vu qu'une grande partie des atomes de Si auront pour voisin une impureté ou du vide. De fait, ces problèmes peuvent être éliminés en utilisant du silicium amorphe (Si-a) produit par implantation d'ions de Si dans du silicium cristallin. Effectivement, il a été montré, à partir de mesure de diffusion de rayons X à petits angles [26], que le Si-a préparé par implantation ionique est complètement homogène et ne présente pas de nano-structure de vide. L'implantation ionique consiste à bombarder avec des ions, dont l'énergie s'étend de quelques dizaines d'eV pour les implantations de surface jusqu'à plusieurs MeV pour les implantations dites à haute énergie, un matériau solide [27-30]. L'implantation de ces ions, sous certaines conditions expérimentales, induit dans les semi-conducteurs des changements topologiques du réseau cristallin de

départ sous forme de changement de phase d'un état cristallin à un état amorphe [31]. L'implantation ionique présente l'avantage d'être une méthode qui produit des matériaux amorphes de haute pureté avec une excellente reproductibilité. De plus, des mesures de concentration atomique sur le silicium amorphe [32,33] ont montré que le silicium amorphe est 1.7 % moins dense que le cristallin.

La seconde raison pour laquelle une RDF du Si-a fiable n'est pas disponible, est que la majorité des mesures expérimentales de diffraction ne couvrent qu'une partie restreinte de l'espace réciproque Q ($Q_{max} \sim 20$ Å^{-1}). Il est à noter que la résolution de la RDF est inversement proportionnelle à la valeur Q_{max} (la borne maximale de l'espace des Q sondé); une résolution de 0.1 Å nécessiterait de balayer une région de l'espace des Q allant jusqu'à 30 Å^{-1}. Dans le but d'outrepasser toutes ces difficultés reliées à l'obtention d'une RDF fiable et précise, nous avons préparé, par implantation ionique et gravure chimique, deux membranes de silicium amorphe pures de ~11 μm d'épaisseur. Alors que le premier échantillon tel qu'implanté n'a subi aucun traitement (état non relaxé), l'autre a été recuit sous vide afin d'atteindre un état de relaxation complet. Au chapitre I, nous présentons un article où sont décrites les différentes étapes de préparation et d'analyse des membranes de silicium amorphe pur utilisées lors des mesures de diffraction de rayons X.

Nous avons alors réalisé des mesures de diffraction de rayons X provenant d'une source de rayonnement synchrotron (CHESS)[3]. Ceci nous a permis de balayer une grande gamme de l'espace des Q allant de 0.5 à 55 Å^{-1}. Nous avons aussi effectué

une mesure similaire, sous les mêmes conditions expérimentales, d'une poudre de silicium cristallin (Si-c) afin de déterminer sa fonction de distribution radiale qui servira de mesure de référence. Aux Chapitres III, nous présentons un article qui rapporte les principaux résultats de ce travail, les différents détails concernant le traitement des données de diffraction et l'analyse des fonctions de distribution radiale, ainsi que des nouvelles techniques concernant le filtrage des transformée de Fourier et la détermination du facteur de diffusion du silicium, f_{Si}, de 0 à 55Å^{-1} .

4- Relaxation structurelle et défauts :

Une des grandes différences entre le silicium amorphe et le silicium cristallin est que plusieurs propriétés physiques bien définies (luminescence, conductivité, enthalpie ..) pour le silicium cristallin s'avèrent être variables pour le silicium amorphe car elles dépendent de sa manière de préparation ainsi que de son historique thermique. La densité du silicium amorphe restant la même après un recuit de 580 °C, les variations des grandeurs physiques du silcium amorphe implanté sont alors intrinsèques à la nature de sa structure atomique.

La transition de la structure du silicium amorphe après implantation à un état relaxé thermiquement est connue sous le nom de relaxation structurelle i.e au cours d'un recuit thermique, il subit une relaxation graduelle vers un nouvel état d'équilibre qui s'accompagne d'un dégagement de chaleur [34]. Ceci a pour effet de diminuer les contraintes emmagasinées dans la structure métastable (telle qu'implantée). Selon une première approche, la relaxation structurelle peut être vue comme un processus où

---

[3] *Cornell High Energy Synchrotron Source*

chaque tétraèdre du réseau amorphe subit une réorganisation locale, ce qui se traduit par une variation au niveau des angles de liaisons tétraédriques, θ, comme l'indique les différentes mesures Raman [35-37]; La déviation angulaire des liens tétraédriques, $\Delta\theta$, (par rapport à θ) passe de 11° pour un échantillon amorphe tel qu'implanté à 9° après recuit thermique. La deuxième approche veut que ce soit l'annihilation des défauts présents dans la structure non relaxée (métastable) qui jouent un rôle dominant lors du processus de relaxation. Plusieurs études ont montré l'existence de défauts dans les matériaux amorphes préparés par implantation ionique [36-39]. Ces défauts peuvent être de même nature ou similaires aux défauts ponctuels qui se retrouvent dans les réseaux cristallins. Dans ce travail, nous verrons que l'analyse des fonctions de distribution radiale du silicium amorphe relaxé et tel qu'implanté montre que les défauts sont impliqués dans le processus de relaxation structurelle dans le silicium amorphe.

CHAPITRE I

Edge Supported Amorphous Silicon Membranes For Diffraction Studies

Auteurs: Sjoerd Roorda, Khalid Laaziri et Subhash C. Gujrathi.

Edge supported amorphous silicon membranes for diffraction studies

Sjoerd Roorda, Khalid Laaziri, and Subhash C. Gujrathi.

Département de physique et Groupe de recherche en physique et technologie des couches minces, Université de Montréal, CP 6128 succursale Centre-ville, Montréal H3C 3J7 Canada

Abstract

Edge-supported membranes of pure amorphous silicon have been prepared by ion implantation and chemical attack. Analysis by elastic recoil detection showed that impurity levels for oxygen and hydrogen are well below 0.1 at. % except in a thin layer at the etched surface. Raman spectroscopy confirmed the amorphous nature of the samples as well as the difference between as-implanted and thermally annealed samples. These samples were later used for X-ray diffraction measurements with the goal of determining reliably the radial distribution function of amorphous silicon with high resolution.

Introduction

The radial distribution function (RDF) is one of the most important properties of an amorphous material since it relates directly to the atomic structure[1]. It is essential that the RDF be known if a thorough understanding of the nature of the amorphous structure itself or that of its structural relaxation and point defect phenomena is to be reached. Experimentally, the RDF is determined by a Fourier transform of the diffracted intensity of X-rays or neutrons and such a measurement obviously requires a sufficient amount of material. In this paper we describe how to make amorphous silicon (a-Si) samples for an experiment aimed at obtaining the RDF but the procedure can, of course, be modified for other materials.

Amorphous silicon is an important model system for all amorphous materials because its basic building block is a single silicon atom. Its structure, and its similarities and differences with crystalline silicon (c-Si), should therefore be relatively easily understood and relate directly to the role of disorder on its (electrical, optical, mechanical, thermal, and so on) properties. Surprisingly, the RDF of pure amorphous silicon is not reliably known in spite of repeated efforts[2-7]. In fact, a number of papers with model calculations on the structure of amorphous silicon[8] compare the calculated RDF with one experimentally determined on amorphous germanium[9].

The paucity of reliable information regarding the RDF of a-Si stems from the difficulty of obtaining sufficient material of high purity and good homogeneity for the

diffraction experiment. Plasma- or chemical vapour deposited hydrogenated a-Si can be of very high quality but contains a few at.% of hydrogen. Amorphous silicon made by sputtering typically contains a similar amount of the sputtering agent, whereas a-Si made by vacuum evaporation tends to peal off the substrate even before the layer thickness reaches one micron. More importantly, almost all a-Si made by deposition techniques contains voids[10] that may reach several nm in size and represent a volume fraction of several %, which means that a considerable fraction of the atoms sits at internal surfaces and not in the bulk. The origin of the void structure may be related to the fact that every atom in the deposited a-Si was a surface atom during some stage of the deposition process. The best way to avoid the inclusion of the voids, therefore, is to prepare a-Si directly from the crystalline or liquid phase.

There are, as far as we can tell, four ways of making a-Si directly from the crystalline or liquid phase. Nano-indentation of crystalline silicon gives, upon sudden release, extremely small amounts of a-Si[11]. The amounts are so small that it is even difficult to establish its amorphous nature. Pulsed laser melting of c-Si can give, if the pulse duration and laser energy density are well chosen, pure a-Si but the layer thickness is only a few nm[12,13]. Ball milling yields large amounts of material but it generally contains so much iron that it is better to speak of amorphous alloys although some relatively pure a-Si has been reported[14]. That leaves ion implantation. MeV self-ion implantation typically gives up to a few microns of a-Si of very good reproducibility. The layer thickness can be increased to 12 μm by increasing the implantation energy to 30 MeV or so. It has been shown conclusively by small angle X-ray scattering that a-Si prepared this way is indeed free of nano-voids[15], even

though its density is a little less than that of c-Si[16]. In this paper, we describe the preparation and characterization of a-Si samples suitable for use in an X-ray diffraction experiment by multi-MeV ion implantation.

Ion implantation

The ion implantation schedule is based on the famous recipe of D.C. Jacobson for the preparation of 2 μm thick a-Si layers[17]. Reproducibility is achieved by cooling the silicon wafer to liquid nitrogen temperature during the ion implantation, by maintaining a power deposition of less than a few W/cm^2, and by an implantation dose that exceeds the threshold for amorphization by a factor of five. The recipe calls for three successive implantations of 5×10^{15} Si ions/cm^2, namely at 500 keV, 1 MeV and 2 MeV. The amorphization takes place most efficiently near the end-of-range, and a logical extension of this recipe for thicker a-Si layer would be to simply add higher energy ion implantations, where each additional implantation step would add a fraction of a μm a-Si (the buried interface between a-Si and c-Si would go a bit deeper at each implantation). The ion doses at each energy were estimated by aiming for a similar nuclear energy deposition as in the end-of-range of the 2 MeV implantation, as calculated by TRIM[18]. This led to the implantation sequence as shown in Table I which calls for a total implantation dose of 8.3×10^{16} Si ions/cm^2 at energies up to 27 MeV.

A potential concern of this method is that the multi-MeV ions passing through the a-Si that already exists somehow induce crystallization or structural relaxation at or near the surface. This could possibly occur as a result of the large electronic energy

loss of these ions. Raman spectroscopy of the ion-implanted surface did not show any sign of crystallization happening. Another concern is the possibility that thin c-Si layers remain between the end-of-range amorphized layers of the last and highest energy implantations, because at the higher energies the separation between the EOR becomes substantial. There was no way to test this other than by the actual X-ray diffraction measurement. No evidence for c-Si remaining between the a-Si layers was found, even in 12 μm thick samples that had been thermally annealed at 600 °C for 1 hour. (Any remaining c-Si seed would have grown to an easily observable crystallite by such a treatment[19].)

The sequence shown in Table I was used to fabricate a number of samples. Some were just a 1 cm² area of a slightly larger rectangular piece of undoped, double sided polished c-Si of 100 μm thickness and these were meant for the X-ray diffraction experiments. Some were kept as-implanted; others were annealed in vacuum at 600 °C for 1 hour. The c-Si backing of these samples was removed as will be discussed in the next section. Other samples were made that were somewhat larger but required no removal of the backside. These were the (300 μm thick, single side polished) samples used in the small angle X-ray scattering experiments, mentioned in the introduction, that showed the absence of voids in this material.

Wet etch by KOH

The X-ray diffraction measurement requires that there are no traces of c-Si exposed to X-rays during the measurement because such traces will introduce Bragg peaks that would have to be removed manually from the data. Therefore, the c-Si

backing has to be removed and this was accomplished by a chemical etch. To this end, the sample was turned upside down and covered with a Teflon container filled with etching solution (20% KOH in water). The container had a small circular hole in the bottom, which was pressed against the c-Si back surface. A cross section of the container, viton and teflon o-rings, and the sample, is shown in figure 1. A series of concentric seals was used since a single o-ring gave unsatisfactory results: leakage between the surrounding hot water and the container occurred and furthermore, relatively large strains accumulated at the single sealing surface which we suspect were responsible for enhanced etch rates around the perimeter of the o-ring. The only way to avoid enhanced etch rates at the o-ring was to use a flat teflon seal.

To facilitate etching, the c-Si starting material was only 100 μm thick and polished at both surfaces. A variety of materials could have been used as an effective etch stop[20], but this would have introduced two problems: first, the deep end of the thick a-Si layer would have to coincide exactly with the beginning (or rather, the near-surface side) of the etch stop and second, some of the etch stop material would inevitably be ion mixed into the a-Si. Instead, the etch speed in c-Si was determined precisely (1.2 μm/min.) and the temperature closely controlled to keep it constant at 80 °C. The etch depth was essentially controlled by carefully timing the chemical attack. It was found that the etch rate of KOH in a-Si is about one-half that of the etch rate in c-Si[21], which helped a lot with the timing of the etch depth. In fact, during the etch, bubbles appeared at a constant rate at the etched surface and a sudden decrease in the rate of bubble formation signaled the arrival of the etch solution at the a-Si. The teflon container was then emptied and the sample removed and cleaned.

The end result of the chemical attack is a circular membrane of pure a-Si that is supported at the edges by the original c-Si sample. These membranes were found to be surprisingly robust; they survived additional ion-beam bombardment and physical transport over many km. The thickness of the membranes is a bit less than that of the original a-Si layer because the etch always removes some of the a-Si. The thickness of each membrane was measured by determining the energy loss of MeV protons passing through the membranes. This was achieved by scattering MeV protons off a piece of Si into a surface barrier detector. The membrane was inserted between the Si piece and the detector and the apparent surface energies of the Rutherford backscatter spectrum with and without membrane were compared. It was found that all membranes had thicknesses between 9 and 11 μm. Because the density of a-Si is slightly less than that of c-Si, the a-Si membranes tend to buckle a little bit because they are larger than the diameter of the etched hole.

Chemical purity

Ion implantation of Si ions into c-Si undoubtedly can produce a-Si of the highest purity but there are two reasons that dictate that the purity of the samples should be verified. One, vacuum or beam problems during the implantation may introduce impurities near the surface and throughout the a-Si. Second, during the chemical attack at 80 °C, impurities could conceivably diffuse into the a-Si back-surface. The chemical purity of the a-Si membranes was verified by elastic recoil detection of 35 MeV Cl ions incident 15° from the surface[22]. Both the front and the back-surface of an a-Si membrane were tested. Hydrogen recoils were separated from

all other recoils by a stopper foil and detected by means of a surface barrier detector. All other elements were detected in the time-of-flight arm of the ERD chamber. In all cases, the outgoing recoils were collected at 15° from the surface; the angle between incident beam and detected recoils was 30°.

Analysis of the time-of-flight spectra and the hydrogen spectrum[23] leads to the data shown in figure 2, which shows all impurities that could be detected at the etched surface. Since some surface roughness remains after the etch, the depth scale is only approximate. Substantial hydrogen and oxygen and some carbon and metallic impurities are observed at the surface and in the first 20 nm but well into the bulk all impurity levels drop to values below 0.1 at.% or the detection limit. The small signal attributed to metallic impurities is likely due to contamination of the etching solution from the chromel-alumel thermocouple. Since the X-ray measurement will probe the entire thickness of the sample (10 μm), the surface contamination is inconsequential. No metallic impurities were observed on the other surface of the membrane.

Structural relaxation and exposure to 60 keV X-rays

One key finding of the X-ray measurements[24] was that the two samples yielded RDF's that were much more similar than expected based on earlier attempts. This raised the question of possible relaxation by the multi-MeV ions passing through the surface or during the chemical attack, or possible relaxation or de-relaxation induced by the X-ray photons. We have therefore determined the Raman spectra at spots on the surface where the X-ray beam had hit the samples. The samples were illuminated with at most 100 mW from an Ar laser at a wavelength of 514.5 nm,

focussed to a size of less than 0.1×0.1 mm^2. The Raman system included a double spectrometer equipped with a single-channel photon counting detector which severely limits the quality of the spectra that can be obtained compared to CCD camera results. However, the spectra do indeed show a difference between the two samples.

Two measured spectra are shown in figure 3. The background was in fact larger than the signal and was removed. This was achieved by measuring the background of a c-Si sample, clipping the sharp peak at 521 cm^{-1} away, and smoothing. The smoothed curve was multiplied with a single normalization constant in order to obtain a signal that could serve as a background for the spectra measured on a-Si. This procedure is not entirely satisfactory and we are planning to undertake additional Raman measurements once the system is equipped with a CCD camera. Raman spectra measured immediately adjacent to the X-ray footprints could not be distinguished from those on the X-ray spot.

The peak positions of the TO-like band of the a-Si samples shifts from 474 ± 3 to 483 ± 2 cm^{-1} upon annealing at 600 ºC, which corresponds very closely to values reported previously[25]. However, at the same time, the half-width at half maximum of the bands decreases only from $36,5 \pm 4$ to 35 ± 3 cm^{-1}, while based on the literature, the widths were expected to decrease from about 42 to 34 cm^{-1}. The error in the values for the band widths is quite large and moreover, the band widths are more sensitive to errors in the background subtraction procedure than the peak positions. The error in the peak positions is also found to be small compared to the difference

between the two peak positions. We tentatively conclude that all of what was mentioned in the first paragraph of this section did not materialize.

Conclusions

In conclusion, edge-supported a-Si membranes of 10 μm thickness have been made by a sequence of MeV ion implantations followed by a KOH chemical attack. The membranes are somewhat buckled and of good mechanical strength. The a-Si of the membranes is of high purity with less than 0.1 at.% contaminants and exhibits, within the limited resolution currently available, the same Raman spectrum as "normal" a-Si. Thermal annealing induces structural relaxation whereas prolonged exposure to X-rays from 13 to 60 keV does not significantly alter the Raman spectrum.

Acknowledgements

References

[1] S.R. Elliott, Physics of amorphous materials

[2] S.C. Moss and J.F. Graczyk, Proc. 10th Int. Conf. Phys. Semicond., ed. S. Keller (Cambridge MA, 1970).

[3] R. Mosseri, C. Sella, and J. Dixmier, Phys. Stat. Sol. (a) **52**, 475 (1979).

[4] A. Menelle, A.M. Flank, P. Lagarde, and R. Bellissent, J. de Phys. **C8**, suppl. au **12**, 379 (1986).

[5] J. Fortner and J.S. Lannin, Phys. Rev. **B39**, 5527 (1989).

[6] J. Fortner and J.S. Lannin, J. Non-Cryst. Solids **106**, 128 (1988).

[7] A. Filipponi, F. Evangelisti, M. Benfatto, S. Mobilio, and C.R. Natoli, Phys. Rev. **B40**, 9636 (1989).

[8] R. Car and M. Parrinello, Phys. Rev. Lett. **60**, 204 (1988).

[9] R.J. Temkin, W. Paul, and G.A.N. Connell, Adv. in Phys. **22**, 581 (1973).

[10] S.C. Moss and J.F. Graczyk, Phys. Rev. Lett. **23**, 1167 (1969).

[11] D.R. Clarke, M.C. Kroll, P.D. Kirchner, R.F. Cook, and B.J. Hockey, Phys. Rev. Lett. **60**, 2156 (1988).

[12] P.L. Lui, R. Yen, N. Bloembergen, and R.T. Hodgson, Appl. Phys. Lett. **34**, 864 (1979).

[13] A.G. Cullis, H.C. Webber, N.G. Chew, J.M. Poate, and P. Baeri, Phys. Rev. Lett. **49**, 219 (1982).

[14] E. Gaffet and M. Harmelin, J. Less-Common Met. **157**, 201 (1990).

[15] D. L. Williamson, S. Roorda, M. Chicoine, R. Tabti, P. A. Stolk, S. Acco, and F. W. Saris, Appl. Phys. Lett. **67**, 226 (1995).

[16] J.S. Custer, M.O. Thompson, D.C. Jacobson, J.M. Poate, S. Roorda, W.C. Sinke, and F. Spaepen, Mater. Res. Soc. Symp. Proc. **157**, 689 (1990), K. Laaziri, S. Roorda, and J.M. Baribeau, J. Non-Cryst. Solids, **191**, 193 (1995).

[17] D.C. Jacobson, Ph.D. Thesis, Stevens Institute of Technology (1988).

[18] J.P. Biersack and L.J. Haggmark, Nucl. Instrum. and Meth. **174**, 257 (1980).

[19] G.L. Olson and J.A. Roth, Mater. Sci. Rep. **3**, 1 (1988).

[20] K. Saitoh, H. Niwa, S. Nakao, and S. Miyagawa, in "Ion Implantation Technology 94", S. Coffa, G. Ferla and E. Rimini, Eds., 998 (Elsevier, 1995).

[21] H. Seidel, L. Csepregi, A. Heuberger, and H. Baumgärtel, J. Electrochem. Soc, **137**, 3612 (1990), and **137**, 3626 (1990).

[22] R. Groleau, S.C. Gujrathi, J.-P. Martin, Nucl. Instr. and Meth. **218** (1983); S.C. Gujrathi, P. Aubry, L. Lemay, J.-P. Martin, Can. J. Phys. **65**, 950 (1987); S.C. Gujrathi, in: Metallization of Polymers, Eds. E. Sacher, J.J. Pireaux, and S.P. Kowalczyk, ACS Symp. Series No. **440**, chap. 6, p. 88 (1990); S.C. Gujrathi, D. Poitras, J.E. Klemberg-Sapieha, L. Martinu, Nucl. Instr. and Meth. B **11**, 560 (1996).

[23] K. Oxorn, S.C. Gujrathi, S. Bultena, L.Cliche, J. Miskin, Nucl. Instr. and Meth. B **45**, 166 (1990).

[24] K. Laaziri, S. Kycia, S. Roorda, M. Chicoine, J.L. Robertson, J. Wang, and S.C. Moss, Phys. Rev. Lett. **82**, 3460 (1999).

[25] S. Roorda, W.C. Sinke, J.M. Poate, D.C. Jacobson, S. Dierker, B.S. Dennis, D.J. Eaglesham, F. Spaepen, and P. Fuoss, Phys. Rev. **B44**, 3702 (1991).

| Ion Energy (MeV)	1.5; 2.0; 3.5	5; 7; 9	11.5; 14; 17; 20	23; 27
Fluence (Si ions/cm^2)	5×10^{15}	6×10^{15}	8×10^{15}	9×10^{15}

Table I. Ion energies and doses used for amorphizing a 12 μm surface layer of c-Si.
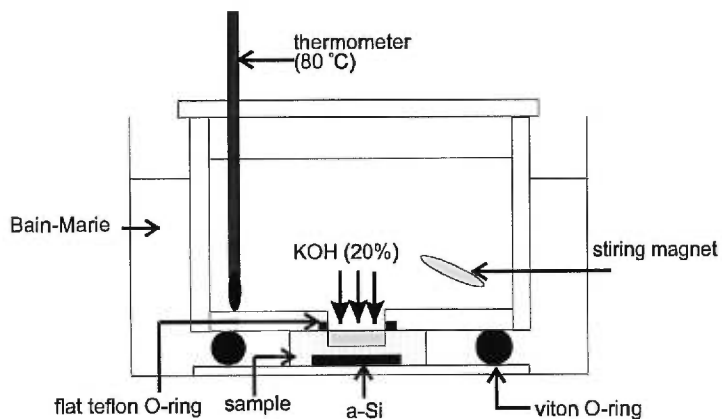
Figure 1. Schematic cross section of the etching apparatus which shows the sample, the teflon container, and the seals. The entire apparatus was submerged in hot water (au bain Marie).
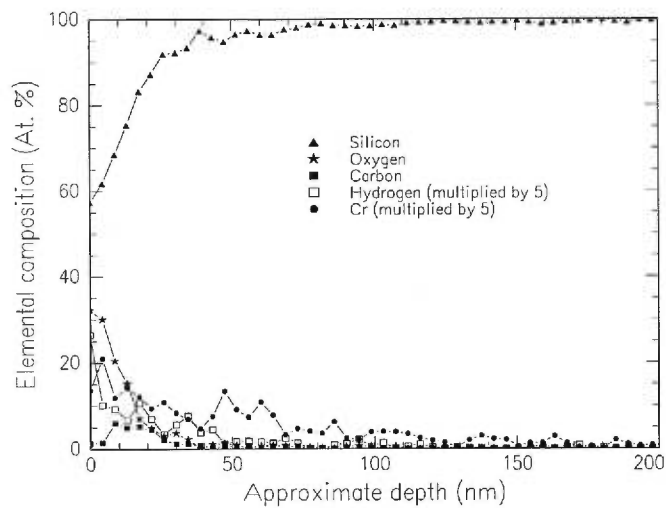
Figure 2. Depth profiles of Si and all detected impurities at the KOH-etched back surface of an a-Si membrane. The depth scale is approximate because of surface roughness. The signals for H and Cr have been multiplied by a factor of 5 for clarity.
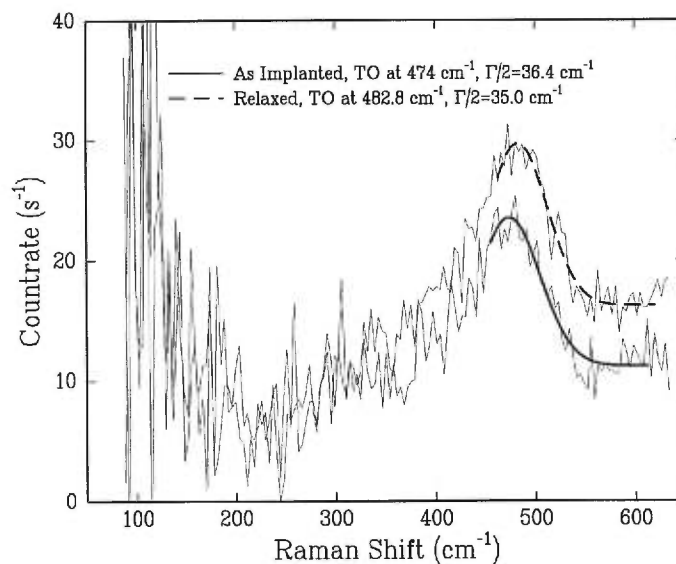
Figure 3. Raman spectra of the a-Si membranes that were used for X-ray diffraction measurements. The Raman laser struck the samples at the same position as previously the X-ray beam.

CHAPITRE II

Quantitative Treatment For Extracting Coherent Elastic Scattering From X-ray Scattering Experiments

Auteurs: Khalid Laaziri , J. L. Robertson , S. Roorda, M. Chicoine, S. Kycia , J. Wang and S. C. Moss.

Quantitative treatment for extracting coherent elastic scattering from X-ray scattering experiments

Khalid Laaziri [1], J. L. Robertson [2], S. Roorda[1], M. Chicoine[1], S. Kycia [3],

J. Wang[4, *] and S. C. Moss[4].

[1]*Groupe de Recherche en Physique et Technologie des Couches minces, Département de Physique, Université de Montréal, C.P 6128 Succursale Centre-Ville, Montréal (QC), H3C 3J7, Canada*

[2]*Solid State Division, Oak Ridge National Laboratory, P.O. BOX 2008, Oak Ridge (TN) 37831-6393, U.S.A*

[3]*CHESS, Wilson Laboratory, Cornell University, Ithaca (N.Y.) 14853, U.S.A.*

[4]*Department of Physics, University of Houston, Houston (TX) 77204-5506, U.S.A.*

[*] present address: *NASA, Houston (TX)*

Abstract

We present a fitting procedure for separating the inelastic and elastic contributions to the total scattering in diffuse scattering experiments at high energy using energy dispersive X-ray techniques. An asymmetric peak function is used to model the elastic peak. The inelastic scattering peak is modeled using a theoretical Compton profile calculated using the impulse approximation (Hartree-Fock wave functions were used), convoluted with the detector resolution. This procedure, which requires only two free parameters, is shown to be extremely effective in extracting the integrated elastic intensity of coherent scattering at each wave-vector, even at low scattering angles where the Compton scattering is not well-resolved.

1. Introduction

The scattering by atoms of X-rays with energies less than 100 keV consists of two main processes. One is the coherent elastic or "Thomson" scattering which occurs when the energy of the incident photon is unchanged after interacting with the atom. This scattering process is responsible for the Bragg reflections that provide information on the atomic structure of a material. The other process is incoherent inelastic or "Compton" scattering. Here the energy of the incident photon is changed after colliding with the atom. For example, a free electron at rest will scatter a photon according to

$$\lambda - \lambda_i = 0.02426 \ (1 - cos2\theta), \tag{1}$$

where λ_i is the incident wavelength, which arises directly from energy and momentum conservation, and 2θ the scattering angle. However, the electrons in the atoms are not at rest, therefore the Compton scattering leads to a distribution of scattered energies superimposed on the elastically scattered signal. Here we include as elastic, the scattering arising from the thermal motion where the energy transfer is very small (meV) compared to the incident energy (keV).

Advances in X-ray sources and instrumentation now allow scattering measurements to be extended out to much larger values of Q, $Q = 4\pi sin\theta / \lambda$. By using 60 keV X rays, data were collected out to Q as high as 60 Å^{-1}, providing an extremely high real-space resolution of the *local atomic structure* of crystalline and amorphous materials. In fact, we have applied the procedure described in this paper to the measurement of the Radial Distribution Function (RDF) of pure amorphous

silicon measured at the CHESS 24-pole wiggler A2-station. As will be shown in forthcoming publications, the combination of a specially prepared sample (very high purity, 10 μm thick, homogeneous, and edge-supported amorphous silicon), large Q range (0.5 to 55 Å^{-1}) and a careful analysis as described here, leads to an RDF of unprecedented precision and resolution.

Such high-energy X rays scattered by thin films have the additional advantage that multiple scattering is negligible; however the new difficulty is the large contribution from the Compton scattering to the total scattering. For amorphous materials composed of light atoms the Compton contribution to the total scattering is often larger than the coherent contribution. In order to extract the integrated elastic scattering, it is important to separate the Compton from the elastic scattering for each value of Q. Many different approaches have been used to resolve this problem. An analyzer crystal with a narrow energy band pass can be used to remove some of the Compton scattering at larger scattering angles, but at low angles the two scattering contributions begin to overlap in energy and cannot be separated in this fashion. Another method consists of collecting the total scattering, normalizing to absolute units, and subtracting the tabulated value for the Compton contribution (*International Tables for X-ray Crystallography*, 1995). There is also the fluorescence excitation method of Warren and Mavel (1965). While in principle these methods will yield an adequate removal of the Compton scattering, in practice great difficulty is encountered when the Compton contribution is large compared to the elastic scattering or when the scattering angle is small. More recently, a very useful method has been developed by Ice and Sparks (Ice & Sparks, 1990) in which a curved mosaic

analyzer crystal focuses the scattered X-rays onto a Position Sensitive Detector (PSD) thereby displaying both elastic and inelastic intensity on a multichannel analyzer. This technique has proved quite useful in the removal of Compton scattering from the diffuse scattering from amorphous materials (Cheng *et al.*, 1994) and disordered crystalline alloys (Reinhard *et al.*, 1992). Its energy resolution is excellent, but it becomes impractical at the very high X-ray energies employed in the present series of experiments.

For our purpose it has proven best to collect the energy spectrum of the total scattering using a germanium solid state detector with a considerably lower energy resolution than that obtained for lower energy using the Ice-Sparks detector (Ice & Sparks, 1990). The scans were performed in reflection and transmission geometry with a fixed incident sample position, and fixed energy of 13, 21.74, and 43.6 keV and by varying scattering angle *2θ*. The germanium detector was calibrated and its resolution was determined using a selection of suitable radioactive sources. The apparent loss of resolution is actually quite acceptable given the extended range of our scans which, as we shall see, permits the complete separation of the Compton and elastic components at high angles for high-energy X-rays. At these energies and angles the analyzer/PSD arrangement cannot properly cover the relevant energy range. Curve fitting of the energy spectrum can then be used to separate the elastic and inelastic contributions. In the following section, we present an accurate and efficient method for modeling the energy spectrum. An asymmetric peak function is

used to fit the elastic contribution, and a calculated Compton profile is used to fit the inelastic contribution to the total scattering.

2. Compton scattering

The energy spectrum of the Compton scattering is calculated using the impulse approximation (Dumond, 1929; Eisenberger & Platzman, 1970). The coupling Hamiltonian for the interaction of the radiation field with a non-relativistic electrically charged particle is given by

$$H = \frac{e}{m_0 c} \vec{p}.\vec{A} + \frac{e^2}{2 m_0 c^2} \vec{A}.\vec{A} \tag{2}$$

by retaining only the A^2, the cross-section for Compton scattering (Eisenberger & Platzman, 1970) is

$$\frac{d^2\sigma}{d\omega d\Omega} = \left(\frac{e^2}{m_0 c^2}\right)^2 \left(\frac{1 + \cos^2 2\theta}{2}\right)\left(\frac{\omega_2}{\omega_1}\right) \sum_2 \left|\langle \Psi_2 | e^{i\vec{k}.\vec{r}} | \Psi_1 \rangle \right|^2 \delta(E_2 - E_1 - \omega) \tag{3}$$

where m_0 is the electron rest mass, 2θ the scattering angle, ω_1 the incident photon energy, ω_2 the scattered photon energy, Ψ_1 and Ψ_2 are respectively the wave functions for the electron in its initial bound state and its final continuum state.

The impulse approximation assumes that the electrons responsible for scattering the photons may be treated as free rather than bound. However, orbital effects are included in so far as they produce a spread in the initial free electron momenta. The cross-section for Compton scattering in this approximation is

$$\frac{d^2\sigma}{d\omega d\Omega} = \left(\frac{e^2}{m_0 c^2}\right)^2 \left(\frac{1 + \cos^2 2\theta}{2}\right)\left(\frac{\omega_2}{\omega_1}\right) \frac{m_0}{|k|} J(q) \tag{4}$$

Where k is the momentum transfer, J(q) is the Compton profile (Biggs *et al.*, 1975), q is the projection of p_l(the individual electron momentum before collision upon a unit vector in the direction of the momentum transfer $k=k_1-k_2$,where k_1 is the incident wave-vector and k_2 the outgoing wave-vector) and is proportional to the separation from the center of the Compton line for scattering from a free electron at rest. It is expressed in atomic units of $me^2/\hbar$ which is the average electron momentum in the ground state of hydrogen,

$$q = -\frac{\vec{k}.\vec{p}_1}{|k|} = -137 \frac{\left[\omega_1 - \omega_2 - \omega_1\omega_2\left(\frac{1-\cos 2\theta}{m_0 c^2}\right)\right]}{\sqrt{\omega_1^2 + \omega_2^2 - 2\omega_1\omega_2 \cos 2\theta}} \qquad (5)$$

$$J(q) = \frac{1}{2}\int_q^\infty \frac{I(p)}{p}dp \qquad (6)$$

I (p) is the electron momentum density for electrons of momentum *p*.

The Impulse Approximation Compton Profiles (IACP) calculated numerically in this paper are based on the work of Biggs *et al.* (1975) using the non-relativistic and relativistic Hartree-Fock wavefunctions of Mann (Mann & Waber, 1973; Mann, 1973). The routine for generating IACP may be obtained on request from the authors (K. Laaziri, S. Roorda). Figure 1 shows an example of the IACP for $2\theta = 90°$ and an incident energy of 40 keV.

3. Thomson scattering

An analytical asymmetric peak function (available in most curve fitting software) was used to describe the elastic scattering. Due to the asymmetry of the

coherent scattering, probably arising from focusing and monochromating system, common peak fit functions cannot adequately reproduce the tails of the elastic peak. The following analytical asymmetric peak function gave satisfactory results,

$$a_0 e^{\left(\frac{a_1 - a_2 \ln(a_3) - x}{a_2}\right)} \left[1 + e^{\left(\frac{a_1 - a_2 \ln(a_3) - x}{a_2}\right)}\right]^{-a_3 - 1} a_3^{-a_3} (a_3 + 1)^{a_3 + 1} \tag{7}$$

where a_0, a_1, a_2 and a_3 are, respectively, the height, center, width, and shape of the peak. Figure 2 shows an example of this analytical peak function.

4. Fitting procedure

The curve fitting procedure consists of five steps:

1. Select an energy spectrum collected at large scattering angle where the elastic and the Compton contributions are well separated (see fig. 3).

2. Calculate the corresponding IACP .

3. Fit the spectrum to determine the Compton amplitude, the elastic peak amplitude (a_0), center (a_1), width (a_2) and shape (a_3).

4. For all other values of Q, calculate the corresponding IACP, and fit to determine the amplitude of the Compton and the elastic contribution, while keeping a_1, a_2 and a_3 fixed.

5. For each spectrum subtract the Compton contribution and integrate to obtain the elastic scattering.

Of course, the first step can be carried out for several spectra collected at large scattering angles in order to determine the parameters a_1, a_2 and a_3 more precisely.

Figures 4 and 5 show some typical fits to energy spectra collected at different scattering angles. We note that with this curve fitting procedure, even when the inelastic and elastic peaks are not well resolved, smooth fits can still be obtained as we can see from fig. 6.

The fitting function used was,

$$F(x) = E(x) + C_o(x) \tag{8}$$

where $E(x)$ is the elastic fitting function (7) with a_0 as the only free parameter, and $C_o(x)$ is the Compton fitting function, expressed as:

$$C_o(x) = N \times Spline(x) \tag{9}$$

$Spline(x)$ is a spline fit of the calculated IACP, and N is a fitting parameter for the Compton amplitude. The theoretical IACP, convoluted with the detector resolution, gives the correct shape of the Compton scattering peak; therefore the only other free parameter (besides a_0) is the Compton scattering amplitude N.

The importance of this procedure is that no systematic errors are introduced during the evaluation of the integrated intensity of the elastic peak. This is not the case for the Single Channel Analyzer (SCA) technique, where discriminator windows are set on the elastic scattering peak so as to exclude incoherent Compton scattering. One can easily show that this method introduces a systematic error varying with 2θ, compared to the method presented here due to an indeterminent amount of the incoherent scattering entering the detector. Table 1 shows the result of the integrated intensity of the elastic scattering peak for different scattering angles, observed during our X-ray diffraction experiment on pure amorphous silicon. Using data collected

with the solid state detector output going simultaneously to the multichannel analyzer and a SCA with the discriminator window centered on the elastic energy. In the first column of Table 1 we show the intensity (integrated over the energy window) from the SCA and in the second column the integrated intensity is deduced from our curve-fitting procedure. At low scattering angle when the peak separation between the elastic and Compton scattering becomes very small, the Compton scattering contributes a substantial amount to the counts within the SCA discriminator window. The error in evaluating the true elastic scattering count is plotted in fig. 7. The systematic error introduced by not discriminating against the Compton contribution increases rapidly towards low scattering angles. This is of great concern because the RDF, especially the RDF at short-range, is very sensitive to systematic errors in the diffracted intensity which vary slowly with Q. Therefore, errors such as those shown in Fig. 7, may be expected to compromise seriously the RDF's determined using only a SCA to suppress the Compton contributions to the total signal. By using the method described in this paper, i.e. measuring and fitting the energy spectrum at each value of Q, such errors can be avoided and a clean and unambiguous elastic scattering profile can be attained.

5. Conclusion

An efficient curve fitting procedure for energy spectra in X-ray scattering has been presented in this paper. This curve fitting method allows the separation of the elastic and inelastic (Compton) scattering intensities, even at very low scattering angles where they are not fully resolved experimentally.

References

Biggs F., Mendehlson L. B., & and Mann J.B., (1975). Atomic Data and Nuclear Data Tables **16,** 201.

Cheng J., Moss S. C., Eisner M., & Zschack P., (1994). Pigment Cell Res. **7**, 255.

Dumond J.W. M., (1929). Phys. Rev. **33**, 643.

Eisenberger P., & Platzman P. M., (1970). Phys. Rev. A **2**, 415.

Ice G. E., & C. J. Sparks C. J., (1990). Nucl. Instr. Methods A **291**, 110.

International Tables for X-ray Crystallography (1995). Vol C. Birmingham : Kynoch Press.

Mann J. B., (1973). Atomic Data and Nuclear Data Tables **12,** 1.

Mann J. B., & Waber J.T., (1973). Atomic Data and Nuclear Data Tables **5**, 201.

Reinhard L., Robertson J. L., Moss S. C., Ice G. E, Zschack P., & Sparks C. J., (1992). Phys. Rev. B **45,** 2662.

Warren B. E., & Mavel G., (1965). Rev. Sci. Instr. **36**, 196.

| 2θ	Elastic intensity from discriminator window (counts)	Elastic intensity from curve fitting (counts)	Error (%) In elastic intensity from discriminator
129	1090	1075	1.4
116	1320	1300	1.5
104	1313	1292	1.6
94	1632	1601	1.9
85	2210	2120	4.2
77	2729	2569	6.2
68	2900	2637	9.9
61	3869	3352	15
53	5185	4182	24
46	7158	5189	38

Table 1. Systematic error introduced into the coherent elastic intensity by using an SCA discriminator with the energy window centered on the elastic energy as compared with fitting the energy spectrum for an incident energy of 21.74 keV.
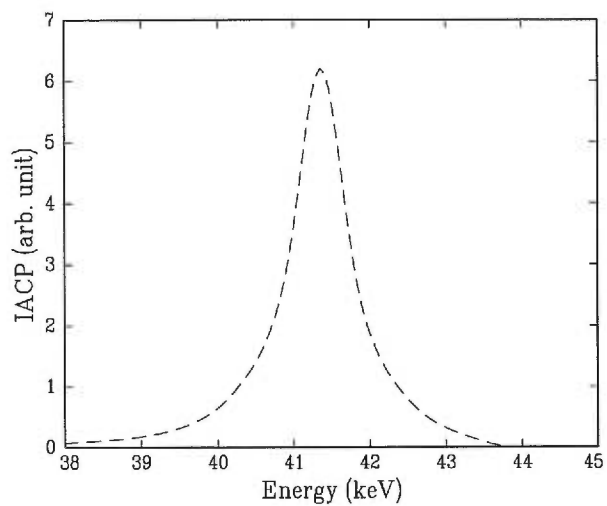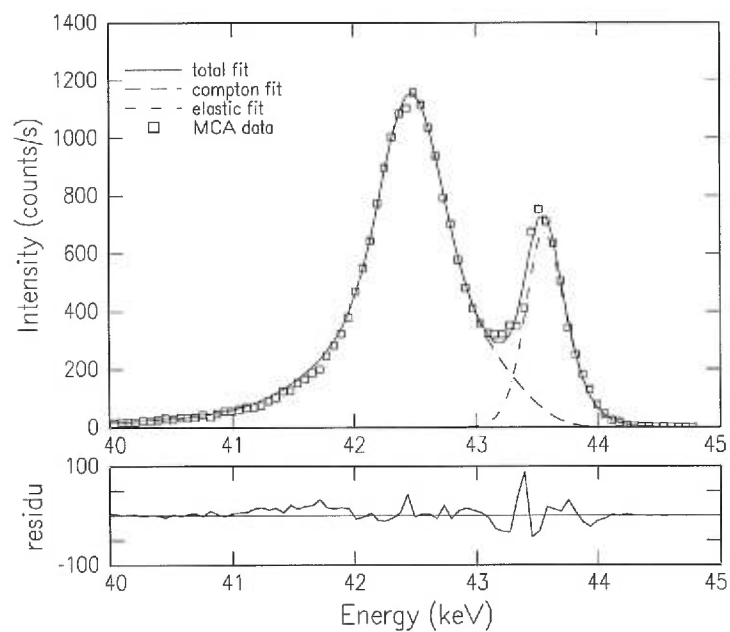
Figure 1. Impulse Approximation Compton Profile calculated for 43.6 keV incident X-ray scattered through 90^0 by amorphous silicon.
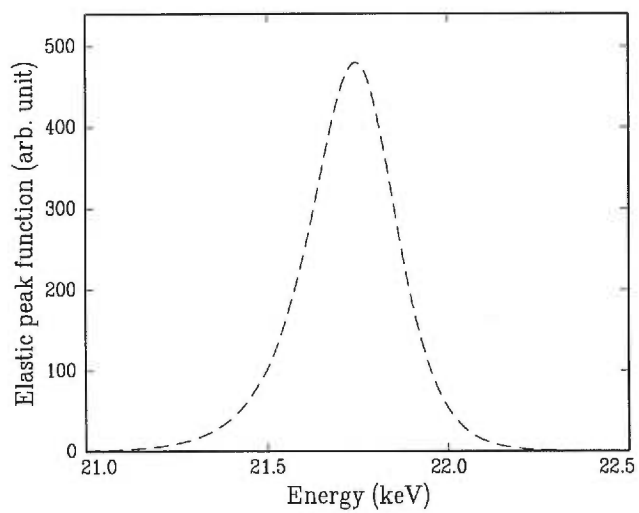
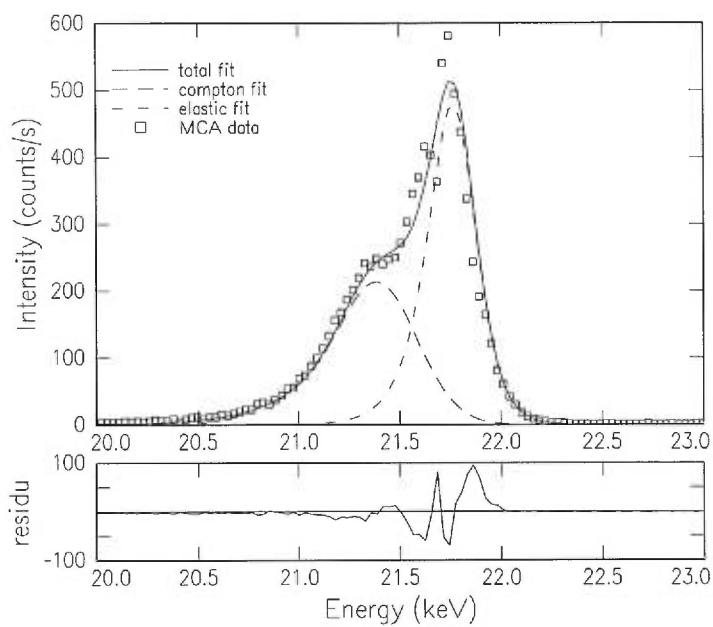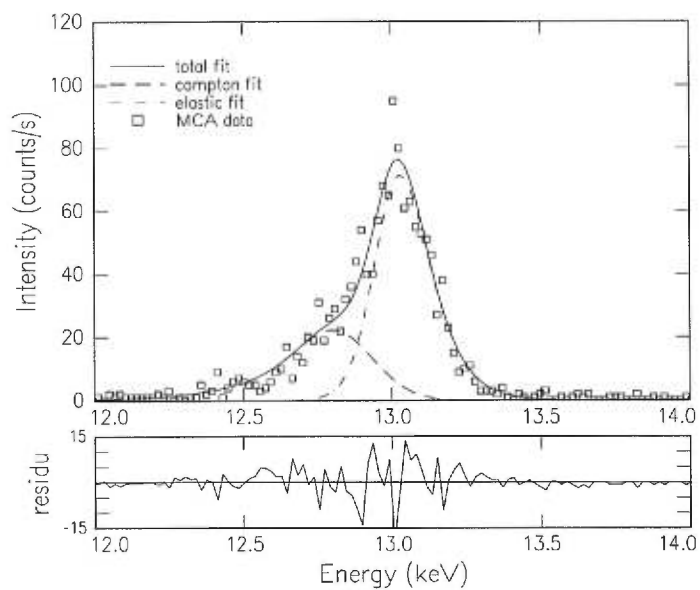**Figure 2.** Asymmetric elastic peak function for an energy of 21.75 keV
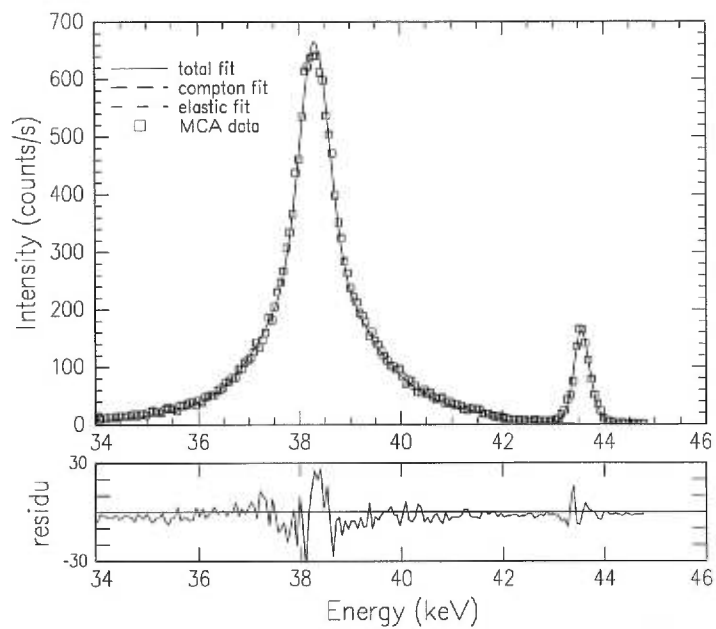
Figure 3 : Fit of the total X-ray scattering energy spectra at Q=40 Å⁻¹ (E=43.6 keV)

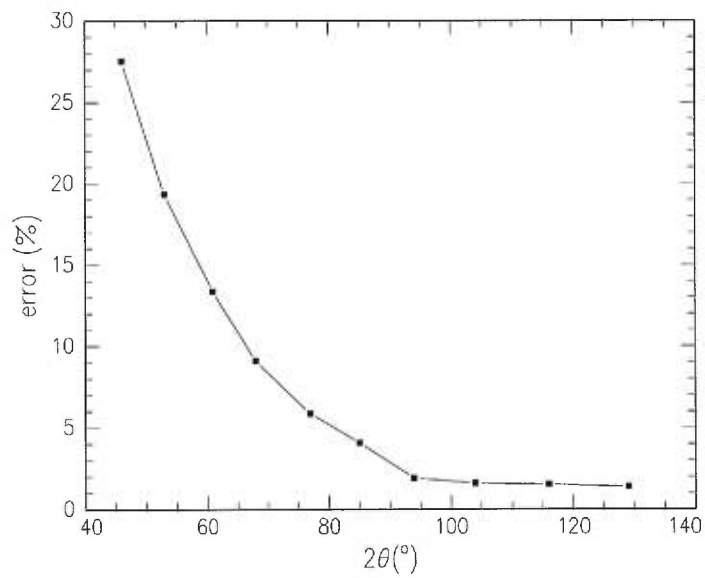**Figure 4** : Fit of the total X-ray scattering energy spectra at Q=20 Å⁻¹ (E=43.6 keV)

Figure 5 : Fit of the total X-ray scattering energy spectra at Q=10 Å^{-1} (E=43.6 keV)

Figure 6 : Fit of the total X-ray scattering energy spectra at Q=7 Å^{-1} (E=13 keV)

Figure 7 : Systematic error in the integrated elastic scattering intensity introduced by using a fixed discriminator energy window.

CHAPITRE III

High Energy X-Ray Diffraction Study Of Pure Amorphous Silicon

Auteurs: Khalid Laaziri , S. Kycia , S. Roorda, M. Chicoine, J. L. Robertson, J. Wang and S. C. Moss.

High-Energy X-ray Diffraction Study Of Pure Amorphous Silicon

Khalid Laaziri[1], S. Kycia[2], S. Roorda[1], M. Chicoine[1], J. L. Robertson[3], J. Wang[4,*] and S. C. Moss[4].

[1]*Groupe de Recherche en Physique et Technologie des Couches minces, département de physique, Université de Montréal, C.P 6128 Succursale Centre-Ville, Montréal (QC), H3C 3J7, Canada*

[2]*CHESS, Wilson Laboratory, Cornell University, Ithaca (N.Y.) 14853, U.S.A.*

[3]*Neutron Scattering Group, Solid State Division, Oak Ridge National Laboratory, P.O. BOX 2008, Oak Ridge (TN) 37831-6393,.*

[4]*Department of physics, University of Houston, Houston (TX) 77204-5506, U.S.A.*

* *currently with Net Explorer, Houston, TX*

Abstract

Medium and high-energy X-ray diffraction has been used to study the atomic structure of pure amorphous Si prepared by MeV Si implantation into crystalline silicon. Both as-implanted and annealed samples were studied. The inelastically scattered X-rays were removed by fitting the energy spectrum for the scattered X-rays. The atomic scattering factor of silicon, previously known reliably up to 20 $\overset{\circ}{A}^{-1}$, has been extended to 55 $\overset{\circ}{A}^{-1}$. The radial distribution function of amorphous Si, before and after annealing, has been determined through an unbiased Fourier transformation of the normalized scattering data. Gaussian fits to the first neighbor peak in these functions shows that scattering data out to at least 40 $\overset{\circ}{A}^{-1}$ is required to

determine the radial distribution function reliably. The first shell coordination number increases from 3.79 to 3.88 upon thermal annealing at 600 °C, whereas that of crystalline Si determined from similar measurements on a Si powder, analyzed using the same technique is 4.0.Amorphous Si is therefore under-coordinated relative to crystalline Si. Noise in the distribution function, caused by statistical variations in the scattering data at high momentum transfer, has been reduced without affecting the experimental resolution through filtering of the interference function after subtracting the contribution of the first neighbor peak. The difference induced by thermal annealing in the remainder of the radial distribution functions, thus revealed, is much smaller than previously believed.

I. Introduction

The atomic scale structure of amorphous solids, which have no spatial periodicity, yields diffuse diffraction patterns. X-ray, neutron, and electron diffraction experiments have been used to characterize the structure of such materials. From the Fourier transform of the diffraction pattern, a correlation function between pairs of atoms, the radial distribution function (RDF), can be deduced. The RDF is, to a certain extent, a very useful representation of the topology of an amorphous network, as it contains information such as the characteristic distances associated with different neighbor pairs, the mean bond angles, and the coordination number of the first neighbor peak. However, it is a one-dimensional representation of the structure of amorphous solids because of their isotropic nature. In order to discern the three-

dimensional atomic structure, one must construct models, such as Continuous Random Network (CRN)[1-2] models hand-built, or computer generated model[3-7] and compare their RDF's with those obtained experimentally. Structural models that are quite distinct may therefore yield RDF's that are only slightly different. Hence, accurate radial distribution functions with high spatial resolution are needed to discriminate among models for the actual atomic structure. This resolution is also essential in revealing subtle differences among samples prepared and annealed in various ways.

Synchrotron radiation sources have made available high intensity photon beams at wavelengths much shorter than those used for conventional X-ray scattering experiments. Thus much larger momentum transfers, $Q = 4\pi sin\theta /\lambda$, are accessible which in turn makes much higher real space resolution of the RDFs possible. In the present study the Q-range was extended to 55 Å^{-1} which corresponds to a real space resolution of 0.1Å. However, the use of high energy X-rays introduces a number of experimental difficulties. At high Q, the Compton contribution to the total scattering is often considerably larger than the coherent contribution for amorphous materials composed of light atoms like Si. In order to extract the integrated elastic scattering, it is important that one be able to separate the Compton from the elastic scattering. Also, the atomic scattering factor for Si, f_{Si}, is not well determined for Q values beyond ~ 20 Å^{-1}. This problem can be dealt with relatively easily for amorphous silicon by using an analytical procedure to extend f_{Si} to larger Q, assuming that the scattering data are sufficiently accurate at high Q. In addition to problems associated

with measurements at high X-ray energy, there are other inherent difficulties that are present when constructing RDFs from the diffraction data. In particular, the Fourier transform of a finite collection of data suffers from termination effects. Which can be reduced by damping functions at the price of reduced spatial resolution. Alternatively, a sampling method can be used. Finally, careful attention should be paid to the accuracy of the instrumental alignment, sample mounting, statistics, correction procedures (dead time, absorption, multiple scattering, and so on), and data analysis as each of these can introduce experimental artifacts in the final RDF[8].

Another aspect of the accuracy of the RDF of amorphous Si involves the obvious need for amorphous material of high purity and good homogeneity for the scattering experiment. Early measurements of the RDF of a-Si[9,10] concluded that evaporated a-Si contains voids. Other studies[11-17] used material containing significant amounts of impurities such as O, Ar, or H. Plasma- or chemical vapor deposited hydrogenated a-Si, though of very high quality electronically, contains by design a few at % of hydrogen. Amorphous silicon made by sputtering typically contains a similar percentage of the sputtering agent, whereas a-Si made by vacuum evaporation tends to peel off the substrate even before the layer thickness reaches one micron. More importantly, almost all a-Si made by deposition techniques contains voids[10,18] that may reach several *nm* in size and represent a volume fraction of several %. This means that a considerable fraction of the atoms sit at internal surfaces and are not fully coordinated. The origin of the void structure may be related to the fact that every atom in the deposited a-Si was a surface atom during some stage of the deposition process. One way to avoid the inclusion of voids is to prepare a-Si directly

from the crystalline or liquid phase. For this study we used MeV self-ion implantation which typically yields only a few microns of a-Si. By using several implantation energies for the silicon ions, the thickness of the amorphous layer can be extended to greater than 10 μm. Recently, small-angle X-ray scattering (SAXS) measurements on a-Si made by such multi-MeV ion implantation[19] demonstrated the void-free nature of this material. Interestingly, studies on a-Si prepared by ion implantation which is free of voids have shown that the amorphous state is less dense[20,21] than the crystalline state with a density deficit of 1.8% for both as-implanted and thermally annealed a-Si.

In this paper, we will describe a detailed study of the determination and analysis of the RDF of amorphous silicon in the as-implanted and annealed states, compared with that of a crystalline silicon powder under similar experimental conditions. The experimental details of the high-energy X-ray scattering measurements covering a Q-range from 0.03 to 55 Å^{-1}, as well as the details of the data analysis will be discussed. In addition, we will present a method for removing the Compton scattering, describe how the atomic scattering factor, f_{Si}, can be extended to larger Q, and demonstrate a procedure for filtering noise from the RDF. Our results show that even for fundamental information such as the nearest neighbor coordination number, diffraction data out to at least 40 Å^{-1} in Q is required. The majority of results presented in the literature (for amorphous materials in general) do not extend beyond 25 Å^{-1}. We find that amorphous silicon is slightly under-coordinated with respect to a fourfold coordinated continuous random network, which explains why amorphous silicon is less dense than its crystalline counterpart. The high resolution RDFs also allow us to resolve a long-standing issue directly related to

the atomic structure of amorphous silicon, namely the nature of the structural relaxation induced by thermal annealing (1 hour at 600 °C)[22]. This structural relaxation can be understood as the removal of about 2 at. % of point self defects, thus contradicting an earlier description of structural relaxation in terms of a reduction in the average bond angle distortion -- a view which implies that every atom contributes equally to the structural relaxation.

II. Experiment

A. Sample preparation

Edge supported amorphous silicon membranes were prepared[23] by implanting undoped silicon substrates with Si^+ ions at different energies and doses (see table I) at liquid nitrogen temperature. The implantations were carried out at the 6 MV Van der Graaff Tandem accelerator located at the *Université de Montréal*. The samples were then chemically etched from the back side of the implanted surface, in order to remove all the crystalline substrate, using a solution of KOH (20%) at a temperature of 80 °C and under continuous magnetic stirring; the etch rate was about 1.2 μm/min. The KOH temperature was held constant during the etching process. This procedure resulted in pure a-Si membranes of 10 and 11 μm thickness as measured by interferometry (FTIR) and energy loss of energetic protons. One of the two samples was then annealed under vacuum at a temperature of 600 °C for 1 hour in order to induce structural relaxation. The other sample remained as-implanted. Raman spectroscopy was performed on the etched interface to make sure that no crystalline material was left. Elastic recoil detection in conjunction with time of flight analysis

was used to check the concentration and the depth profile of trace elements at the etched interface, and it was found that, apart from a small surface contamination, the concentration of C, O, and H was less than 0.1 at. %.

After the chemical etch, a slight buckling was observed of both membranes. Because a-Si is less dense than c-Si, both the amorphous film and the underlying substrate are somewhat stressed after the ion implantation. From wafer-curvature measurements during the implantation, it has been shown that the stress is largest just before a continuous amorphous is layer is formed, and that the stress relaxes through viscous flow of the a-Si (even at liquid nitrogen temperatures) during and immediately after the implantation[24]. However, not all the stress is relieved, and we observe that after removal of the crystalline backing, the membranes are indeed slightly larger than the circular hole they are spanning, which leads to the slight buckling of the membranes. Both membranes (as-implanted and annealed) were similarly buckled. The X-ray scattering was performed roughly in the middle of the membrane, far from the edges, where the stress should be almost completely relieved. Raman scattering on these same positions (reported in ref. [23]) showed a TO-like band (and shift induced by annealing) as would normally be observed in a-Si. We believe, therefore, that mechanical stress does not play a significant role in the different atomic structures observed here. In fact, since the majority of work on a-Si concerns thin films on a substrate, mechanical stresses should play a much smaller role here, than in almost all experimental results published to date.

High-purity silicon powder (reference 640b from the National Institute of Standards and Technology) with an average particle diameter less than 10 μm was

used as a crystalline reference sample. The silicon powder was pressed onto a 1.5 cm diameter polished disk (thickness of 2 mm). A solution of 1 % of solvent based adhesive, diluted with acetone, was used to hold the fine silicon particles together. Since only a very small amount of the solution was used, less than 1 ml, the scattering from the adhesive can be safely ignored.

B. X-ray diffraction

The experimental arrangement for the diffraction measurements is shown schematically in Fig. 1. It incorporates a focusing and monochromating system which consists of a Si(111) double-bounce monochromator with a sagittally bent second crystal for focussing the X-ray beam down to 1 mm height. The slits (S_1 and S_2) just before the sample were used to define a 1 mm high and 3 mm wide incident beam. A NaI scintillator placed between S_2 and the sample was used as a monitor. The samples were placed in a Displex cryostat (Model CSA-202A) mounted on a Huber 6-circle diffractometer to cool the samples to 10 K in order to minimize thermal atomic vibrations, which damp the structure factor $S(Q)$ and thus broaden the peaks in the RDF. The sample holder system was covered by a beryllium can under vacuum, to prevent condensation and air scattering.

The measurements on a-Si were carried out at the station A2-wiggler beamline of the Cornell High Energy Synchrotron Source (CHESS, Wilson laboratory). In order to cover the large region in Q-space from 0.5 to 55 Å^{-1}, four X-ray energies (13, 21.74, 43.57 and 60.1 keV) were used in reflection and, for the low Q scans, transmission geometry. With this choice of energy and geometry, it was always

possible to resolve experimentally the incoherent Compton scattering from the coherent elastic scattering. The Q-scans were taken at regular intervals ΔQ=0.025 Å^{-1}. Table II summarizes the experimental configuration of this experiment. The Q-range measured at each energy was chosen to have overlapping regions between the scans. During each measurement the sample position was maintained at a fixed angle ϕ (angle between the incident beam and the sample). The scattered X-rays were detected using an intrinsic Ge solid state detector with a 160 eV resolution. The signal from the detector was processed by a multi-channel analyzer (MCA) and a complete energy scan was recorded for each value of Q, thus allowing the Compton scattering to be removed.

The powder diffraction measurements on crystalline silicon were carried out at the CHESS C station using a 40.7 keV X-ray beam. The same experimental setup described above for the amorphous samples was used for this experiment, except that the measurements were all done in transmission. Two sets of multiple scans were performed: First, a Q range from 8 to 35 Å^{-1} was covered at regular Q steps of $\Delta Q =$ 0.01 Å^{-1}, then a second one for low Q scans from 1.5 to 10 Å^{-1} at $\Delta Q = 0.005$ Å^{-1}. For the second series of scans, the beam was attenuated so that the Bragg peaks did not saturate the solid state detector. The powder scans were performed using a $\theta \, / \, 2\theta$ geometry with an offset applied to the sample angle, $\phi = \theta + \textit{offset}$, where θ is half the scattering angle 2θ. The offset was varied for each scan by 2° to a total range of $\pm$ 8° in order both to minimize texture effects often observed for powder crystalline samples and to obtain a better powder average.

For both the amorphous and crystalline Si measurements, multiple scans were recorded. Each scan had sufficient counting statistics for a full analysis including the Fourier transform and peak fitting of the resulting radial distribution functions. This allowed us to determine the variance in the fitting results and use those to estimate the incertainty in the final results.

III. Data analysis

The corrected intensity for both the amorphous and the crystalline powder samples is of the form

$$I_{corr} = \frac{I_{exp}}{M(\theta)A(\theta)V(\theta)}\left[\beta + \frac{(1-\beta)}{P(\theta)}\right] \tag{1}$$

where I_{exp} is the experimentally measured elastic intensity corrected for background, dead time, and, for the crystalline Si, multiple scattering and illuminated volume as well. β is the fraction of polarized X-rays ($\beta = 0.93$ for A2 station and $\beta = 0.85$ for C station), $M(\theta)$ the multiple scattering, $A(\theta)$ the absorption, $P(\theta)$ the polarization, and $V(\theta)$ the volume correction. For amorphous silicon, $V(\theta) = 1$ since there was no need for this correction. Each of these correction terms are discussed in the following sections.

Background and dead time correction

In order to make accurate corrections for the instrumental background, some measurements were made with the sample removed, but with the full sample environment in place including the sample holder. In general, the dead time correction factor for the counting system used can be expressed as:

$$C_T = \frac{C_o}{1 - C_o\tau} \tag{2}$$

where C_T, C_o are the true and observed number of counts in the detecting system respectively and τ is the dead time constant. Both the monitor and the solid state detector were corrected for dead time. The respective dead time constants τ_m and τ_d were determined by the multiple-foil method[25,26]. Typically, $\tau_m \sim 6$ μs, while the values for τ_d values were ranging from 15 to 30 μs for the range of X-ray energies used during the experiment.

Compton correction

The Compton inelastic scattering intensity $I(Q)$ was subtracted from the experimental MCA energy spectra using a fitting procedure developed previously[27]. Basically, the MCA spectra were fit using a function of the form $F(x)=E(x)+C_o(x)$ where $E(x)$ is an asymmetric peak function corresponding to the elastic peak and $C_o(x)$ is a theoretical Compton profile derived from the impulse approximation[28-30]. The shape parameters for the asymmetric peak function were only determined once for each X-ray energy, whereas the Compton profile was calculated for each scattering angle 2θ. The fits to the energy spectra were achieved with only two free parameters, namely the amplitudes of the elastic and Compton contributions. The amplitude of the Compton scattering was included in the fit because, although the impulse approximation gives accurate shapes for the Compton scattering profile as a function of 2θ, it underestimates the intensity at large Q. Figures 2 and 3 show examples of the fits for low and high Q scans. After fitting each energy spectrum,

$C_o(x)$ was subtracted from the spectrum and the spectrum was integrated to get the true experimental elastic scattering intensity. The purpose of the asymmetric peak function was solely to aid in the separation of the Compton and elastic contributions.

Multiple scattering

A multiple scattering correction was performed to obtain the experimental singly scattered elastic intensity[31,32]. The following correction was used:

$$I_{exp\,single} = \frac{I_{mes}}{(1+R)} \tag{3},$$

where I_{mes} is the experimentally measured elastic intensity and $R = I_{mult}/I_1$ is a calculated ratio between double and single scattering (courtesy of Simon Billinge, Michigan State University). The multiple scattering correction is applied to the elastic intensity only, before the absorption and polarization corrections. For the thin amorphous silicon membranes the multiple scattering is completely negligible, but for the much thicker crystalline powder Si sample it amounted to $\sim 2\%$ of the elastic intensity.

Absorption

X-rays passing through a sample are partially absorbed by an amount depending on the total path length of the incident and scattered beam. Therefore a correction to the measured intensity must be applied. The absorption correction for both the reflection and transmission geometry has been deduced from the general expression,

$$A(\theta) = \frac{1}{V} \int_V e^{-\mu(L_1 + L_2)} dV \tag{4}$$

where V is the illuminated volume of the sample and L_1 and L_2 are the incident and scattered path lengths. For the reflection geometry,

$$A(\theta) = \frac{s}{V\mu} \frac{\sin(2\theta - \phi)}{\sin(2\theta - \phi) + \sin\phi} \left[1 - e^{-\mu t \left(\frac{1}{\sin\phi} - \frac{1}{\sin(2\theta - \phi)} \right)} \right] \tag{5}$$

and for the transmission geometry

$$A(\theta) = \frac{s}{V\mu} \frac{\sin(\phi - 2\theta)}{\sin(\phi - 2\theta) - \sin\phi} \left[e^{-\frac{\mu t}{\sin(\phi - 2\theta)}} - e^{-\frac{\mu t}{\sin\phi}} \right] \tag{6}$$

where s is the cross-section of the incident beam, V the sample volume, μ the absorption coefficient, t the thickness of the sample and ϕ the incident angle. The factor μt has been measured for the amorphous and powder crystalline silicon samples at each of the energies used during the experiment and are listed in table III. Typically, the absorption corrections were in the order of 3 % for the a-Si samples, and 12% for powder c-Si.

Volume correction

A volume correction is needed to correct for the fraction of irradiated volume seen by the detector as defined by the slits in front of the detector, and it varies with scattering angle, 2θ,

$$V(\theta) = \frac{1}{2} \left[\frac{l^2}{\sin\theta\cos\theta} - \tan\theta \left(\frac{l}{\sin\theta} - t \right)^2 \right], \qquad \theta < \theta_c \tag{7}$$

$$= \frac{1}{2} \frac{l^2}{\sin\theta\cos\theta} \qquad , \qquad \theta > \theta_c \tag{8}$$

where $l = 1$ mm is the vertical height of the incoming beam, $t = 1.7$ mm the thickness of the c-Si powder sample and $\theta_c = 36^o$ is the critical angle where the irradiated volume becomes smaller than that defined by the detector slits. This correction was not needed for the a-Si samples, because the area defined by the detector slits was larger than the irradiated volume in all the range of scattering angles 2θ.

Polarization factor

The X-rays were highly polarized (around 90 % for beamline station A2, and 85 % for station C). Once the majority of the corrections were applied to the intensity data, we used the fraction of polarized X-rays as a free parameter (within limits) to adjust the overlap between the Q-scans corresponding to the different energies. A value of 93 % turned out to give the best agreement between the overlap regions for a-Si (station A2), and 85 % for c-Si powder (station C). The remaining intensities, 7 % and 15 % for the a-Si and the powder c-Si sample respectively, were then corrected for polarization using the factor,

$$P(\theta) = \frac{\left(1 + \cos^2 2\theta\right)}{2} \tag{9}$$

Typically, the polarization corrections were of the order of 3 % for a-Si, and 8 % for the c-Si powder.

Verification of correction procedure

Figure 4 shows the different overlap regions obtained by matching the corrected intensities for a-Si. It can be seen that the overlap between the different

regions is good to within 1%, indicating that the various corrections were applied correctly. In order to illustrate the effects of errors that might be introduced by a problem with one of the corrections, we arbitrarily changed the fraction of polarized X-rays β, by ± 5 %. The error introduced into the polarization correction by reducing β by 5 % and its dramatic effect on the overlapping regions are shown in Fig.5. However, when β is increased by 5 % the polarization correction still seems to give satisfactory results. In summary, this test indicates that the scattering data are sensitive to small errors in the correction procedures. Fortunately, the overlapping regions will usually indicate when there is a problem.

Atomic scattering factor

In order to normalize the corrected intensity I_{corr} to electron units (e.u.), we needed to deduce an atomic form factor for Si, f_{Si}, from the data. f_{Si} is reliably known up to $Q \sim 20$ Å^{-1} and this was used as a starting point. The elastic scattering intensity from the amorphous samples oscillates around f^2 until the oscillations die out at large Q. f_{Si}^2 was expanded to larger Q, as follows:

1- We used the previously determined value[33] of f_{Si} from 0 to 20 Å^{-1} to roughly normalize the data to e.u. The normalization factor was calculated following the method of Krogh-Moe[34] and Norman[35].

2- A new intensity is constructed as illustrated in Fig.6. From 0 to 20 Å^{-1} the intensity was replaced by f_{Si}^2, from 20 to 30 Å^{-1} the original scattering data was retained, and from 30 to $Q_{temp} = 35$ Å^{-1} (a temporary maximum) the scattered intensity was replaced with heavily smoothed data. This fabricated intensity was

then fit using a series of exponential functions; the resulting fit corresponds then to a new, interim f_{Si}^2. Steps 1 and 2 are repeated iteratively by varying the value of Q_{temp} from 35 Å^{-1} until the whole range is covered (0-55 Å^{-1}). Using the literature value for f from 0 to 20 Å^{-1} forces the expanded f to coincide with the literature value in that range.

3- The resulting function was then fit by a monotonically decreasing analytical

function $f(Q) = c + \sum_{i=1}^{5} a_i \exp(-b_i Q^2)$ (11),

in order to avoid spurious effects due to statistical variations during the process.

The fitted parameters are listed in Table IV. With this single set of parameters, the scattering data from both a-Si and the powder c-Si samples could be satisfactorie analyzed.

Fourier transform and termination ripples

The structure factor is defined as $S(Q) = \left(\dfrac{I(Q)}{f^2} \right)$ (12)

where $I(Q)$ is the fully corrected and normalized coherent scattering intensity.

The interference function is defined as, $F(Q) = Q \times [S(Q)-1]$ (13)

The Fourier transform of the structure factor, $G(r)$, called the reduced radial

distribution function, is given by $G(r) = \dfrac{2}{\pi} \int_0^{\infty} Q(S(Q)-1) \sin Qr dQ$ (14)

from which we derive the radial distribution function, $J(r)$,

$J(r) = 4\pi r^2 \rho(r) = 4\pi r^2 \rho_o + rG(r)$ (15)

and $T(r) = 4\pi r \rho_o + G(r)$ (16)

where $\rho(r)$ is the number density function of the actual atomic structure and ρ_o is the average atomic density of the sample.

The ideal Fourier transform of $Q(S(Q)-1)$ in principle requires data from $Q = 0$ to $Q = \infty$. However, the range of Q values achieved experimentally is limited to a finite value, Q_{max}. This cut-off the data will introduce 'termination ripples' of wavelength $2\pi/Q_{max}$ into the RDF and causes a broadening of $J(r)$ due to the cut-off function, $H(Q)$,

$$H(Q) = 1, \quad 0 < Q < Q_{max} \tag{17}$$
$$= 0, \quad Q > Q_{max}$$

Consequently, the actual $G(r)$ obtained by Fourier transforming the experimental data

is given by $G(r) = \dfrac{2}{\pi} \displaystyle\int_0^{\infty} H(Q)Q(S(Q)-1)\sin QrdQ$ \hfill (18)

In other words the measured $G(r)$ is a convolution of the true correlation function and

the peak function, $P(Q) = \dfrac{1}{\pi} \displaystyle\int_0^{\infty} H(Q)\cos QrdQ$ \hfill (19)

The peak function, $P(Q)$, with a peak height of Q_{max}/π and a FWHM (Full Width at Half Maximum) of $3.8/Q_{max}$, yields a broadening of $\Delta r = 0.07$ Å when $Q_{max} = 55$ Å^{-1}. This broadening occurs in each peak of $J(r)$.

The problem of termination ripples can be lessened, to a certain extent, in several ways. Many authors have used damping functions when dealing with termination ripples where they multiply the interference function $F(Q)$ with a modification function $M(Q)$ in order to obtain a gradual cut-off. This procedure

replaces the sharp discontinuity at Q_{max} by a more smoothly varying function. Two common damping functions are used in reducing termination ripples: One is the Lorch function[36]

$$M(Q) = \frac{Q_{max}}{\pi Q} \sin\left(\frac{\pi Q}{Q_{max}}\right) \text{ for } 0 < Q < Q_{max}, \text{ and} = 0 \text{ for } Q > Q_{max}. \tag{20}$$

in which case the corresponding peak function $P_L(Q)$ has a FWHM of $5.437/Q_{max}$, broadening the real space resolution to $\Delta r = 0.098$ Å when $Q_{max} = 55$ Å^{-1}. The other damping function often used is the exponential function[37]

$$M(Q) = exp(-BQ^2) \text{ for } 0 < Q < Q_{max}, \text{ and} = 0 \text{ for } Q > Q_{max} \tag{21}$$

There is no consensus as to the most appropriate value of B in the literature; in most cases, B is chosen so that $M(Q_{max})=0.1$ or less. These methods do indeed reduce the termination ripples, but at a price of broadening the peaks in $J(r)$.

An alternative to the use of damping functions is the so-called "sampling" method[38]. Here, we only use interference functions, $F(Q)$, that terminate with a value of 0 or a maxima or minima at the upper integration limit. In other words, the RDF is calculated only for r values which satisfy the following condition that

$$r = n\frac{\pi}{Q_{max}} \quad \text{or} \quad r = (2n+1)\frac{2\pi}{Q_{max}} \quad \text{where } n = 1,2,3\ldots$$

In these cases every point in the RDF is thus the result of an unbiased Fourier transform of the $S(Q)$ data and no damping function is used. The density of points in real space is limited because of the restrictions imposed by the sampling procedure. However, in reality, it reflects the true spatial resolution. In practice the use of the sampling method should only be considered if the scattering data cover a sufficiently

large region of Q-space to get a sufficiently dense set of points in $J(r)$. Since our data extend to 55 Å^{-1}, use of the sampling method is appropriate.

IV. Results

A. Powder crystalline silicon

In order to test the accuracy of the procedure for determining the RDF of a-Si, the RDF of c-Si was determined through diffraction measurements of a crystalline powder sample (described in the sample preparation section) for Q between 1 and 35 Å^{-1}.

Fig.7 shows the structure factor of c-Si, which includes both Bragg peaks and diffuse scattering contributions. The Bragg peak intensities are likely to suffer from preferred orientation effects, since it is difficult to obtain powder samples with completely random orientation. The Fourier transform, $G(r)$, of the crystalline powder data calculated using the sampling method is shown in Fig.8. For $r < 2$ Å, $G(r)$ oscillates around $-4\pi\rho_o r$, where $\rho_o = 0.04997$ Å^{-3} is the known average atomic density of c-Si. The large oscillation near $r = 0$ (dashed line) is attributed to slowly varying errors in $F(Q)$ and is likely due to an error in the normalization constant. In order to correct for this problem, we have used a procedure due to Kaplow[39]. The low r region ($< r_{min} = 1.5$ Å) of $G(r)$ was Fourier transformed, and subtracted from $F(Q)$; the resulting $G(r)$ is shown as a solid line in Fig.8. The solid and dashed lines overlap everywhere except at $r < 2$ Å, which indicates that the correction only affects the low r region without changing the RDF peaks containing the structural information.

A direct comparison between our data from the sampled Fourier transform and the known structure of c-Si is shown in Fig.9. Here, the solid line is the *J(r)* for the diamond structure with a lattice constant of 5.431 Å, where each peak is broadened to have a Gaussian distribution. For the first peak σ was ~ 0.06 Å and for the other peaks ~ 0.08 Å (nearest neighbors do not vibrate with the same amplitude as uncorrelated distant neighbors). The broadening is a combined effect of thermal disorder and the experimental resolution of the Fourier transform. The dots represent a single sampled point of the Fourier transform. All the points fall quite close to the solid line (and continue to do so much beyond the maximum range of 10 Å shown here). In particular, the positions and heights of the first two peaks are in excellent agreement with the solid line as will be discussed further in the section "coordination vs Q_{max}" where the effect of Q_{max} on the results is examined. This coincidence leads us to conclude that high-energy X-ray diffraction, as analyzed by the method described in this paper, yields an accurate and reliable determination of the RDF.

B. Amorphous silicon

The corrected and normalized elastic intensities *I(Q)*, of both the as-implanted (dotted line) and annealed (solid line) amorphous silicon are shown in Fig.10. Clearly, *I(Q)* oscillates about f_{Si}^2 until the oscillations damp out at large *Q*. The two intensities are almost identical, except at low *Q*, indicating differences in the atomic structure beyond the first neighbor distance. These normalized intensities were used to determine the interference functions, *F(Q)*, for both materials. We have added results from earlier Small Angle X-ray Scattering (SAXS) measurements[19] to the

high-energy synchrotron data in order to achieve a total Q range from 0.03 to 55 Å^{-1}. In Fig. 11, we display the structure factor, $S(Q)$, as determined for both the annealed and as-implanted a-Si. The inset shows the corresponding interference function, $F(Q)$. Oscillations in structure factors are clearly visible up to ~ 40 Å^{-1}. Beyond this value the statistical noise drowns out the oscillations. Again a small difference can be seen between the two structure factors at low Q as noted above.

Fourier transform and noise reduction

The Fourier transform, $G(r)$, calculated for both the as-implanted and annealed a-Si samples using the sampling method is shown in Fig.12. For $r < 2$Å, both curves oscillate linearly around $-4\pi\rho_o r$, where ρ_o is the average atomic density. By least squares fitting, it was deduced that $\rho_o = (0.0489 \pm 0.004)$ Å^{-3}, a value that was identical for the two materials to within 0.1 % and which is in excellent agreement with previous density measurements of a-Si[20,21] where $\rho_o = 0.0492$ Å^{-3}. In $G(r)$, we can see the presence of noise, which we attribute to the statistical noise in $F(Q)$ for large Q, as well as a significant ripple throughout, due to the way the data was binned. Realising that it is primarily the first neighbour peak that determines $S(Q)$ for Q beyond 20 Å^{-1}, we have adopted the following procedure to reduce this noise and ripple: The first neighbour peak in the RDF was isolated and its contribution to the interference function evaluated through a reverse Fourier transform. This contribution was subtracted from the interference function, and the remaining signal which, beyond $Q = 20$ Å^{-1}, is essentially statistical noise only, is damped through multiplication by a factor $exp(-\alpha(Q/Q_{max})^2)$, where $\alpha = 8$, and $Q_{max} =$

55 Å^{-1}. The unfiltered first neighbour contribution is then added back to the filtered data, as illustrated in Fig.13 which shows both the filtered (dotted line) and the unfiltered (solid line) $F(Q)$. The resulting interference function is then Fourier transformed to yield the new filtered $J(r)$. Figure 14 shows $J(r)$ for both materials, filtered (solid line) and unmodified (dots). This filtering procedure was efficient in suppressing the noise from J(r), without affecting the resolution and without altering the termination ripples inherent in the Fourier transform.

In Fig.15, we show the resulting RDF's of both the annealed and the as-implanted a-Si samples from 1 to 5 Å. The first neighbor peaks of both samples are nearly indistinguishable. Note that the height of the second neighbor peak increases upon thermal annealing. Surprisingly, the widths of the second neighbor peaks remain almost identical. In the region between the second and third peak, at around 4.7 Å, a small enhancement in the annealed RDF over the as-implanted RDF can be seen. This observation suggests the existence of a peak seen earlier by Moss and Graczyk[9]. We do not believe that this peak is spurious, since it appears at the same position in all the RDF's calculated using different values of Q_{max}. The existence of such a peak can be indicative of dihedral bond angle ordering[40,41] (the dihedral angle is defined as the angle of rotation about a common bond of two tetrahedral units). In fact, it seems that there is a preferential orientation of the neighboring tetrahedral unit in the annealed a-Si, which is reflected by a narrower distribution, compared to the as-implanted a-Si where the dihedral angle distribution should be quite large. (This peak may also be construed as a weak tendency of a-Si to reflect the third neighbor peak of c-Si[2])

Peak fitting

A full interpretation of the RDF requires extensive modeling of the atomic structure, but basic structural data of the short-range atomic order can be extracted by simply fitting the individual peaks of the RDF - at least those that can be resolved. Since the first peak of the RDF of both crystalline and amorphous silicon is well separated from all the other peaks, the average coordination number, C_1, of the first neighbor Si-Si atom distribution can be evaluated with reasonable accuracy by fitting both $J(r)$ and $T(r)$ to a Gaussian profile. We also used a peak fitting function, corresponding to the contribution of the first peak in Q space, in order to fit $F(Q)$.

The fitting function for $T(r)$ was of the form, $t_i(r) = \dfrac{C_i}{r} \dfrac{e^{-\frac{(r-r_i)^2}{2\sigma_i^2}}}{\sqrt{2\pi\sigma_i^2}}$ \hfill (22),

for $J(r)$ of the form, $j_i(r) = r\, t_i(r)$ \hfill (23),

and for $F(Q)$ (Q space) of the form, $f_i(Q) = C_i \dfrac{\sin r_i Q}{r_i} e^{-\frac{1}{2}Q^2\sigma_i^2}$ \hfill (24),

where C_i is the coordination number in the i-th shell, r_i the position of the i-th distribution, and σ_i^2 is the mean square amplitude of thermal vibration plus mean square static disorder. Fits to $F(Q)$ were done using data starting at 15.2 Å^{-1} in order to allow only contributions from next-neighbor distances. A typical real space fit of $J(r)$ and $T(r)$ is illustrated in Fig.16.

The results of all the curve fits are listed in Table V. For both the as-implanted and the annealed a-Si samples the first neighbor peaks were centered at $r_1 \sim 2.35$ Å and their total widths were $\sigma_1 \sim 0.065$ Å. A small but significant difference occurred

in the coordination numbers, which were $C_1 \sim 3.79$ for the as-implanted sample, and $C_1 \sim 3.88$ for the annealed sample. Table V also lists incertainties; these are determined from the variance of independent fits to five separate RDF's of each sample. The position, coordination number, and the peak widths as determined from the fits of $J(r)$ and $T(r)$ were found to be equal to within 0.1%.

For the second neighbor peak of the a-Si samples, the parameters are difficult to obtain since it contains contribution from more distant neighbor peaks. A crude estimation can be made by first assuming that the second neighbor distribution is symmetric about r_2, and then considering only the lower half of the peak which, to a certain extent, contains only the contribution from the second neighbor correlations. Within the estimated errors, mainly introduced by choosing the upper r cut-off value between 3.75 and 3.9 Å, our best estimate of the a-Si second peak position was $r_2 \sim$ 3.8 Å. The coordination numbers were significantly different with $C_2 \sim 12.15$ for the as-implanted a-Si and $C_2 \sim 12.43$ for the annealed a-Si. The peak widths of the second neighbor peaks were $\sigma_2 \sim 0.258$ Å for the as-implanted a-Si and $\sigma_2 \sim 0.240$ Å for the annealed a-Si.

V. Discussions

There are three main aspects of the results shown in the preceding sections that we wish to discuss further. First, the extent of our data and the simplicity of the material studied allow us to evaluate the reliability and precision of the different approaches to the Fourier analysis. Second, we can begin to examine the atomic structure of a-Si. We will examine the structure of annealed a-Si, which is believed to

be the material closest to an ideal, four-fold coordinated continuous random network. Third, we will examine the changes in the structure of a-Si induced by thermal annealing.

Reliability of radial distribution functions: Coordination vs Q_{max}

As a test of the accuracy of the coordination number it is important to consider it as a function of Q_{max} because it is sensitive to artifacts introduced by cutting off the Fourier transform at Q_{max}. In an earlier publication[42], we showed how the first neighbour peak in the radial distribution function evolves as Q_{max} is increased from 20 to 50 Å^{-1}. In Fig.17, the variation of the coordination number of the first peak, C_1, is shown as a function of Q_{max}. The coordination number of each sample initially decreases with Q_{max}, and then approaches a constant value around $Q_{max} \sim 40$ Å^{-1}. Although the data on the c-Si powder only extend to $Q_{max} = 35$ Å^{-1}, it is clear that the coordination number approaches a value of 4.0. For the smaller values of Q_{max}, the fitting procedure described above overestimates the coordination number because of the contribution from termination ripples. For large Q, the peak shape becomes independent of Q_{max}, with a mean value C_1 of 3.79 ± 0.01 for the as-implanted sample, and 3.88 ± 0.01 for the annealed sample. Beyond $Q_{max} \sim 40$ Å^{-1}, we believe that the intrinsic value for the position, coordination number, and width has been reached. This would indicate that even for a simple, single atom system such as a-Si, reliable RDF's require scattering intensity data that extend to at least 40 Å^{-1}.

Figure 18 illustrates the reliability (or lack thereof) of Lorch (eq. 20, open squares) and exponential (eq. 21, filled squares) damping functions. The figure shows

the values obtained for C_1 by performing Gaussian fits to the first neighbour peak in RDF's calculated using one of the damping functions, again as a function of the upper integration limit Q_{max}. Fitting a Gaussian to a damped transform is effectively equivalent to fitting directly a peak-function, as defined by Warren[43], to an undamped RDF containing termination ripples. The figure also shows the variation in C_1 as a function of Q_{max} for sampled Fourier transformations (star symbols) for as implanted a-Si (Fig. 18 a) and annealed a-Si (Fig. 18 b). All methods converge to the same value at large Q_{max}, reinforcing our confidence in the experimental results. For small values of Q_{max}, < 30 Å^{-1}, the estimates of C_1 based on damped functions seem to give values that approach the final C_1 more closely than that based on a sampled Fourier transform. However, our results do call into question the *reliability* of damping functions. In one sample (Fig 18 a), exponential damping gives a very good estimate but the Lorch-type damping is in error, while in the other sample (Fig 18b), the Lorch-type damping estimates the final value correctly but exponential damping is off by a few percent. When scattering data beyond, say, 30 Å^{-1} are not present, one wouldn't know which method gives the best estimate. Estimates based on sampled transforms at least overestimate C_1 by similar amounts in both samples.

Atomic structure of annealed amorphous Si material

The Gaussian fits to the nearest neighbor peak give an average bond length of (2.350 ± 0.001) Å, compared to our measurement in c-Si of (2.355 ± 0.004) Å. The a-Si bond length is, therefore, identical to that in c-Si to within 0.005 Å. There is, of

course, some static disorder. The width of the first neighbor peak is partially due to this static disorder with additional contributions from thermal disorder and experimental resolution. The last two contributions can be estimated by considering the corresponding value for c-Si where the width of the first peak should be dominated by the thermal motion and real space resolution. We find a peak width of 0.057 Å for the c-Si powder. Assuming that the three contributions are independent, the corrected bond length variation in annealed a-Si is estimated to be 0.031 Å. This small value illustrates the stiffness of the covalent Si-Si bond.

If the small difference in bond length, 0.005 Å, were the only difference between a-Si and c-Si, then a-Si would be 0.6% denser than c-Si, but this is not what is observed. Both our present data (Fig. 12) and macroscopic density measurements[20,21] on void-free a-Si have shown that it is roughly 2 % *less* dense than c-Si. This can now be understood as a consequence of under-coordination. The number of nearest neighbors C_I, obtained from Gaussian fits to the radial distribution function as described above, was found to be 3.88 ± 0.01, significantly less than 4. There are two different ways of accommodating such an undercoordination in an otherwise fully connected fourfold coordinated network. (1) If the undercoordination is solely due to *isolated* dangling bonds, then this number would imply a dangling bond density of 12 %. (2) if the undercoordination is uniquely caused by network vacancies, then this number corresponds to 1 vacancy per 67 network sites (with "vacancy", we mean an unoccupied network site; the four dangling bonds pointing into such a vacancy are expected to rearrange in various ways. Such network vacancies are surprisingly similar to the lattice vacancy in c-Si[44]). To put these two

extreme views in context, we first realize that an *isolated* dangling bond density of 12 % is clearly much higher than what is experimentally observed. It is known from optical absorption[45], electrical[46], SAXS[47], and combined Raman and positron lifetime measurements[48], that only a few at. % H is required to saturate all dangling bonds. The required vacancy density of 1.5 % is, however, much more reasonable as it corresponds closely to the density deficit of a-Si with respect to c-Si. Furthermore, a large number of experiments have shown that a-Si contains vacancy type defects, and that dangling bonds are rarely isolated but mostly associated with structural defects (see also the section below on structural relaxation). We therefore conclude that the undercoordination is mostly due to the presence of vacancy-type defects that result in the density deficit of a-Si with respect to c-Si.

The interpretation of the second neighbor peak in the RDF is less certain because it suffers from an unknown contribution of the third neighbor peak (Fig 16). In the context of a random network containing vacancies, the coordination number of the second neighbor peak C_2 would be approximated by $C_2=C_1\times[C_1-1]$, yielding a value of $C_2 = 11.18$, whereas Gaussian fits yield a value of 12.4 ± 0.4 atoms. The discrepancy could be due to the aforementioned contribution from the third peak, an asymmetry in the second peak, or to a deviation from the network structure. The width of the second peak $\sigma_2 \sim 0.240$ Å contains static disorder (arising from bond length *and* bond angle distortions), thermal vibration and experimental resolution. The thermal contribution can be subtracted from σ_2, again using the powder c-Si results, yielding $\sigma_{2,st} = 0.23$ Å which would imply an average bond angle distortion of

$\Delta\theta_b = (9.63 \pm 0.08)°$. This value for $\Delta\theta_b$ is not unlike values reported in previous studies[10,14,15,16,17,29], but nevertheless should be treated with some caution. The position of the second neighbor peak was found to be at $r_2 \sim 3.8$ Å, which corresponds to an *average* bond angle of $\theta_b = (107.83 \pm 0.97)°$. In the radial distribution function of c-Si, where the second and third peaks are well-separated, $r_2 \sim 3.84$ Å, corresponding to $\theta_b = 109.3°$. Again, the discrepancy could be due to a contribution from the third peak, an asymmetry in the second peak, or to a deviation from the ideal network structure. We once again stress that the analysis of the second neighbor peak and beyond can be more reliably studied through computer modeling rather than through curve fitting.

Structural relaxation and defect annihilation.

The purpose for studying two a-Si samples, one "as-implanted" and the other annealed at 600 °C, is to provide a comparison of their respective atomic structures and draw conclusions regarding the nature of the structural relaxation induced by annealing. At the outset, it should be pointed out that structural relaxation is not densification, as the atomic density of ion implanted a-Si is known to remain unchanged upon annealing to within 0.1 %[20,21,24]. This is confirmed by our measurements, as both samples exhibit the same average density (see Fig. 14). (Densification can be observed in a-Si prepared by deposition techniques, if the growth conditions were such that a nano-porous structure was produced[9].)

Comparing the nearest neighbor peak in the RDF's from both a-Si samples, it is seen that the position and width remain unchanged (to within a 1/1000 of an Å), but

that the area of the peak increases by 2 %, from 3.79 to 3.88 atoms. A host of other techniques has shown that structural relaxation is accompanied by a reduction in the defect density of 2 %, namely isothermal and scanning calorimetry[49], positron spectroscopy[50], Pd solubility and diffusivity measurements[51], and hydrogen trapping[45]. This observation strongly implies that the increase in coordination number is a direct consequence of the reduction in defect density and reinforces our earlier conclusion that the final undercoordination indicates a remaining vacancy density of about 1.5 %. However, it raises the question why structural relaxation is not accompanied by densification. It also raises the confusing question how the difference in coordination between a-Si and c-Si can be related to a density difference (see the discussion above) while at the same time, a similar difference between relaxed and as-implanted a-Si does not lead to a density difference. One possible explanation could be the presence of interstitial type defects, because it is known in c-Si that the volume change induced by equal numbers of vacancies and interstitials is essentially zero.

Interstitial type defects would introduce atomic distances well removed from the main peaks in the RDF but would be difficult to observe because they represent a small fraction of the total number of atom pairs and the distances involved would not tend to peak sharply about any particular value. We have made an attempt to detect such interstitial type defects in our RDF's by subtracting the Gaussian peak profiles from the fits to the first two peaks. Integrating the remaining RDF between the central positions of those peaks would give the added contributions from noise, termination ripples and interstitial type defects. Over a large enough region (from 2.35 to 3.84 Å,

for example), the noise and termination ripple contribution should cancel, and only the contribution from the interstitial type defects would remain. This procedure gave integrated values of about 0.12 and 0.07 atoms for as-implanted and annealed a-Si, respectively. (In c-Si, with much stronger termination ripples, the same procedure yields 0.03 atoms.) If these numbers do indeed represent interstitial type defects, then the increase in coordination number induced by thermal annealing is balanced by a decrease in interstitial defects, thus conserving, as observed, the average atomic density.

The Gaussian fit to the second neighbor peak is less reliable than that to the first, but we estimate that the reliability problem is less serious for comparison purposes between the two a-Si samples than for absolute results. We thus compare the parameters of the second neighbor peak from the two samples and observe that the peak position remains essentially unchanged after annealing, but both the area and the width change. The peak area increases upon thermal annealing, from 12.15 to 12.4 atoms. In the context of defect removal from an otherwise fully connected network, one would expect that C_2 again can be approximated by $C_2 = C_1 \times [C_1 - 1]$. Thus we expect C_2 to increase from 10.45 to 11.18 atoms, based on the first neighbor coordination number in both samples. The observed increase in C_2 is not as large as estimated, and this could be due to a contribution from interstitial type defects or to the general unreliability in the Gaussian fits to the second peak, or both.

The other major difference between the second neighbor peak in our two samples is its width. It is seen that the peak width decreases significantly, implying a

reduction in the average bond angle distortion induced by thermal annealing from $(10.45 \pm 0.09)°$ to $(9.63 \pm 0.08)°$. We attribute the excess in distorted bonds to strained regions surrounding the defects[52,53] in as-implanted a-Si. Annihilation of the defects removes the strained regions, thus reducing the average bond angle distortion.

Earlier experimental work on structural relaxation of a-Si either detected the average bond angle distortion (Raman spectroscopy or low-resolution diffraction), or probed changes in the defect population (positron spectroscopy, carrier lifetime, impurity trapping and diffusion). The high-resolution radial distribution functions presented here allow us to study both aspects, the defect removal (nearest neighbor coordination number increase) and the associated reduction in average bond angle distortion (width of second peak) in one measurement.

Conclusions

In conclusion, we have presented a detailed account of our X-ray diffraction study of the atomic structure of pure amorphous Si. Multi-MeV ion implantation and a wet chemical etch have been used to prepare edge-supported membranes of pure amorphous Si that are free of impurities, crystalline inclusions, and voids. X-ray diffraction has been performed at 13 to 60 keV photon energies up to a scattering vector of 55 $Å^{-1}$. By recording and curve-fitting the scattered energy spectrum at each scattering angle, the Compton incoherent scattering could be separated from the elastic signal carrying the structural information. Using the existing atomic factor f_{Si} of solid Si and our new data, which oscillates slowly around f_{Si}^2, we have extended f_{Si} from 20 to 55 $Å^{-1}$. The extended range over which data were gathered allowed the

use of the sampling method to obtain an unbiased Fourier transformation for the determination of the radial distribution function. Gaussian fits to these functions showed that the nearest neighbor distance in amorphous Si is identical to that in crystalline Si to within 0.005 Å and that the r.m.s static disorder in bond length amounts to ~ 0.03 Å. Both the bond length and its static distortion remain essentially unchanged upon thermal annealing at 600 °C, but the nearest neighbor coordination number increases by 2% from 3.79 to 3.88, which still is one vacancy per 67 atoms short of perfect fourfold coordination. This under-coordination explains why amorphous Si is less dense than crystalline Si. The increase in the average number of nearest neighbors, and other subtle changes in the radial distribution functions induced by thermal annealing, are consistent with an explanation of structural relaxation in amorphous Si in terms of the removal of 2 at. % of point defects.

Acknowledgments

References

[1] D. E. Polk, J. Non-Cryst. Solids **5**, 365 (1971).

[2] D. E. Polk and D. S. Boudreaux, Phys. Rev. Lett. **31**, 92 (1973).

[3] F. Wooten, K. Winer and D. Weaire, Phys. Rev. Lett. **54**, 1392 (1985).

[4] T. Uda, Solid State Commun. **64**, 837 (1988).

[5] I. Stich, R. Car et M. Parrinello, Phys. Rev. B **44**, 11092 (1991).

[6] M. Ishimaru, S. Munetoh et T. Motooka, Phys. Rev. B **56**, 15133 (1997).

[7] N. Mousseau et L. J. Lewis, Phys. Rev. Lett. **78**, 1484 (1997).

[8] B. J. Thijsse, J. Appl. Cryst **10**, 61 (1984).

[9] S.C. Moss and J. F. Graczyk, Phys. Rev. Lett. **23**, 1167 (1969).

[10] S.C. Moss and J. F. Graczyk, *Proceedings of the Tenth International Conference on Physics of Semiconductors*, Cambridge, MA, edited by S. P. Keller, J. C. Hesnel and F. Stern (U. S. Atomic Energy Commission, Washington, DC, 1970), p. 658.

[11] G.A.N Connell, and R. J. Temkin, Phys. Rev. B **9**, 5323 (1974).

[12] S. Kugler, G. Molnár, G. Petö, E. Zsoldos, L. Rosta, A. Menelle and R. Bellissent, Phys. Rev. B **40**, 8030 (1989).

[13] S. Kugler, L. Pusztai, L. Rosta, P. Chieux and R. Bellissent, Phys. Rev. B **48**, 7685 (1993).

[14] J. Fortner and J. S. Lannin, Phys. Rev. B **39**, 5527 (1989).

[15] R. Mosseri, C. Sella, and J. Dixmier, Phys. Stat. Sol. (a) **52**, 475 (1979).

[16] A. Menelle, A. M. Flak, P. Lagarde, and R. Bellissent, J.de Phys. C **8**, suppl. au **12**, 379 (1986).

[17] A. Filipponi, F. Evangelisti, M. Befatto, S. Mobilio, and C. R. Natoli, Phys. Rev. B **40**, 9636 (1989).

[18] I. Ohdomari, M. Kakumu, H. Sugahara, M. Mori, T. Saito, T. Yonehara and Y. Hajimoto, J. Appl. Phys. **52**, 6617 (1981).

[19] D.L. Williamson, S. Roorda, M. Chicoine, R. Tabti, P.A. Stolk, S. Acco, and F. W. Saris, Appl. Phys. Lett. **67**, 226 (1995).

[20] J.S. Custer, M.O. Thompson, D.C. Jacobson, J.M. Poate, S. Roorda, W.C. Sinke, and F. Spaepen, Mater. Res. Soc. Symp. Proc. **157**, 689 (1990).

[21] K. Laaziri, S. Roorda, and J.M. Baribeau, J. Non-Cryst. Solids **191**, 193 (1995).

[22] S. Roorda, W. C. Sinke, J. M. Poate, D. C. Jacobson, S. Dierker, B. S Denis, D. J. Eagelsham, F. Spaepen, and P. Fuoss, Phys. Rev. B **44**, 3702 (1991).

[23] S.Roorda, K. Laaziri, and S. Gujrathi, Nucl. Instr & Methods B **148**, 360 (1998).

[24] C. A. Volkert, J. Appl. Phys. **74**, 7107 (1993).

[25] J. W. Müller, Nucl. Instr. And Methods, **112**, 47 (1973).

[26] D. R. Chipman, Acta Cryst. A **25**, 209 (1969).

[27] K. Laaziri, J. L. Robertson, S.Roorda, M. Chicoine, S. Kycia, J. Wang, and S. C. Moss, J. Appl. Cryst. **32**, 322 (1999).

[28] J.W. M. Dumond, Phys. Rev. **33**, 643 (1929).

[29] P. Eisenberger, and P. M. Platzman, Phys. Rev. A **2**, 415 (1970).

[30] J. B. Mann., and J.T. Waber, Atomic Data and Nuclear Data Tables **5**, 201 (1973).

[31] G. Malet, C. Cabos, A. Escande, and P. Delord, J. Appl. Cryst **6**, 139 (1973).

[32] R. Serimaa, T. Pitkänen, S. Vahvaselkä, and T. Paakari, J. Appl. Cryst **23**, 11 (1990).

[33] D. Waasmaier, and A. Kierfel, Acta Cryst. A **51**, 416 (1995).

[34] J. Krogh-Moe, Acta Cryst. A **9**, 915 (1956).

[35] N. Norman, Acta Cryst. A **10**, 370 (1957).

[36] E. Lorch, J. Phys. C **2**, 229 (1969).

[37] L. W. Bragg and J. West, Philos. Mag. **10**, 823 (1930).

[38] R. Lovell, G. R. Mitchell, and H. Windle, Acta Cryst. **A35**, 598 (1979).

[39] R. Kaplow, S. L. Strong, and B. L. Averbach, Phys. Rev. **138**, A1336 (1965).

[40] R. J. Temkin, W. Paul, and G. A. N. Connell, Adv. Phys. **22**, 581 (1973).

[41] R. J. Temkin, J. Non-Cryst. Solids **28**, 23 (1978).

[42] K. Laaziri, S. Kycia, S. Roorda, M. Chicoine, J.L. Robertson, J. Wang, and S.C. Moss, Phys. Rev. Lett. **82**, 3460 (1999).

[43] B.E. Warren, "*X-ray diffraction*", Dover, New York, 1969, 1990.

[44] G.N. van den Hoven, Z.N. Liang, L. Niesen, and J.S. Custer, Phys. Rev. Lett. **68**, 3714 (1992).

[45] K. F Heidemann, M. Grüner, and E. te Kaat, Rad. Eff. **82**, 103 (1984).

[46] S. Coffa, and J.M. Poate, Appl. Phys. Lett. **59**, 2296 (1991).

[47] S. Acco, D. L. Williamson, P. A. Stolk, F. W. Saris, M. J. van den Boogaard, W. C. Sinke, W. F. van der Weg, S. Roorda, and P. C. Zalm, Phys. Rev. B **53**, 4415 (1996).

[48] Y. Hiroyama, T. Motooka, R. Suzuki, Y. Hirano, and F. Sato, Appl. Phys. Lett. **68**, 3126 (1996).

[49] S. Roorda, S. Doorn, W. C. Sinke, P. M. L. O. Scholte, and E. van Loenen, Phys. Rev. Lett. **62**, 1880 (1989).

[50] S. Roorda, R.A. Hakvoort, A. van Veen, P.A. Stolk, and F.W. Saris, J. Appl. Phys. **72**, 5145 (1992).

[51] S. Coffa, J.M. Poate, D.C. Jacobson, and A. Polman, Appl. Phys. Lett. **58**, 2916 (1991).

[52] A. Antonelli, E. Kaxiras and D. J. Chadi, Phys. Rev. Lett. **81**, 2088 (1998).

[53] H. Seong and L. J. Lewis, Phys. Rev. B 53, 9791 (1996).

Ion Energy (MeV)	0.5;1.5; 2.0; 3.5	5; 7; 9	11.5; 14; 17; 20	23; 27
Fluence (Si ions/cm^2)	5×10^{15}	6×10^{15}	8×10^{15}	9×10^{15}

Table I. Ion energies and doses used for amorphizing a 12 μm surface layer of c-Si.

Region	I	II	III	IV	V
2θ (^{o})	59-130	45-130	54-130	44-129	4-57
Q (Å^{-1})	30-55	17-40	10-20	4.9-11.9	0.5-6.25
ΔQ (Å^{-1})	0.025	0.025	0.025	0.025	0.025
E (keV)	60.1	43.569	21.74	13	13
Geometry Φ (^{o})	Reflection 44°	Reflection 44°	Reflection 44°	Reflection 40°	Transmission 100°

Table II. Experimental parameters for X-ray scattering of amorphous silicon.

Energy (keV)	60	43.569	21.74	13
μ (cm^2 / g)	0.0164	0.490	3.7718	13.643

Table III. Experimentally determined absorption coefficient for silicon.

| Parameters	Deduced f (0 - 55 Å^{-1})
c	0.207976
a_1	3.67842
a_2	3.84222
a_3	1.56637
a_4	0.528977
a_5	4.17884
b_1	3.31157
b_2	41.2418
b_3	0.091511
b_4	131.486
b_5	1.49295

Table IV. Coefficients for the analytical expression of the scattering factor of silicon.

|	As-implanted a-Si			Annealed a-Si			Crystalline powder Si	
	$t(r)$	$j(r)$	$f(Q)$	$t(r)$	$j(r)$	$f(Q)$	$t(r)$	$j(r)$
C_1	3.786±0.01	3.79±0.01	3.787±0.12	3.882±0.01	3.881±0.01	3.886±0.12	4.032±0.04	4.021±0.05
r_1	2.349±0.001	2.351±0.001	2.349±0.04	2.351±0.001	2.352±0.001	2.351±0.004	2.354±0.003	2.356±0.004
σ_1	0.064±0.001	0.064±0.001	0.064±0.003	0.065±0.001	0.065±0.001	0.065±0.003	0.057±0.003	0.0569±0.004
C_2	9.57±0.20	12.15±0.11	-	9.71±0.11	12.43±0.38	-	12.16±0.23	12.15±0.22
r_2	3.795±0.01	3.808±0.01	-	3.80±0.01	3.81±0.01	-	3.84±0.002	3.841±0.002
σ_2	0.259±0.006	0.257±0.006	-	0.242±0.008	0.238±0.006	-	0.066±0.002	0.066±0.002

Table V. Peak fitting parameters for annealed, and as-implanted amorphous silicon ($Q_{max} = 55$ Å^{-1}), and crystalline powder silicon ($Q_{max}=35$ Å^{-1}).
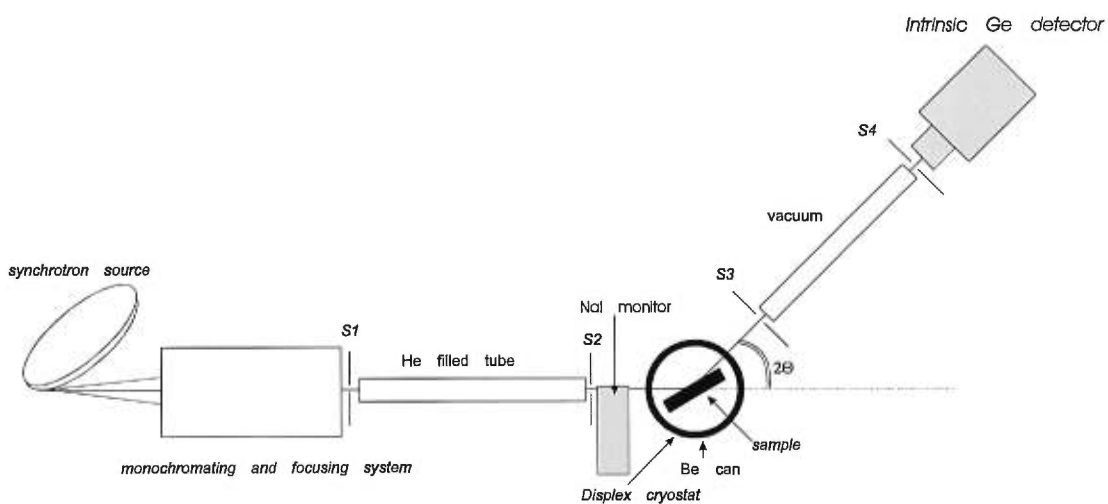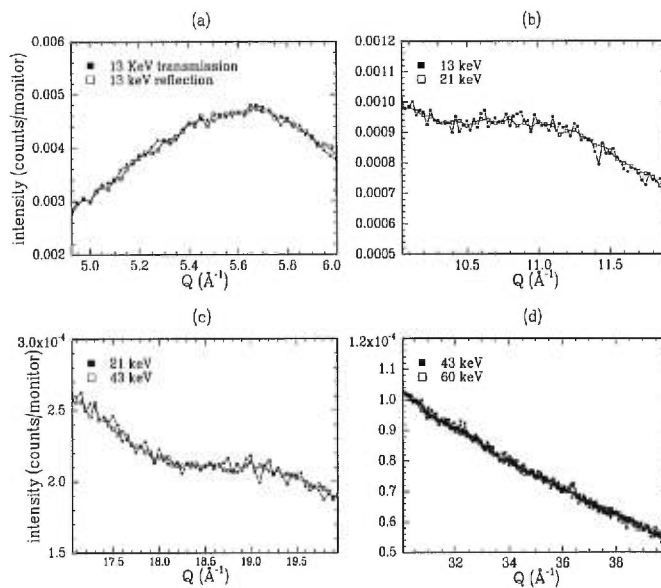
**Figure 1**. The schematic diagram of the experimental configuration for this experiment.
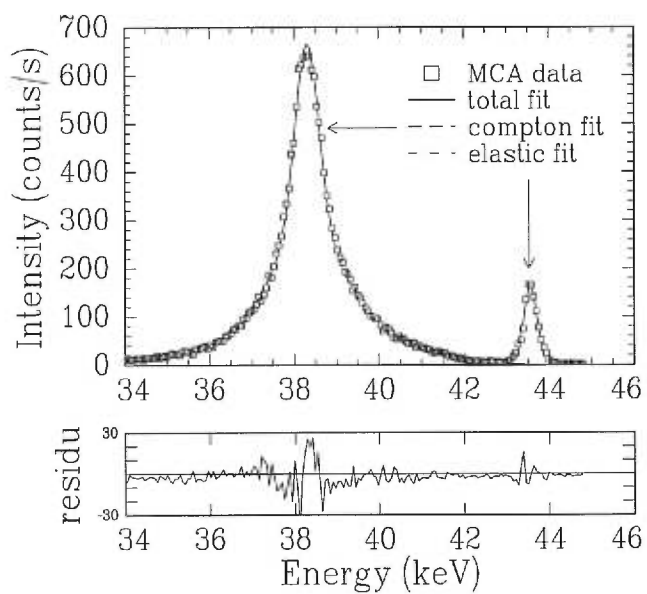
**Figure 2.** The fit of the total X-ray scattering energy spectra at $Q = 40$ Å^{-1} (E=43.6 keV).
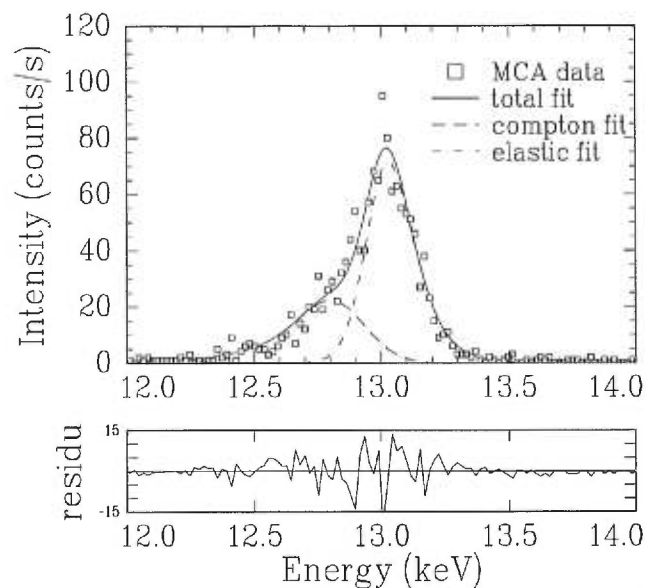
Figure 3. The fit of a total X-ray scattering energy spectrum at $Q = 7$ Å^{-1} (E=13 keV)


Figure 4. The amorphous silicon intensity overlap regions for the different energies used in this diffraction experiments: (a) between 13 keV transmission and reflection, (b) between 13 keV, and 21 keV reflection, (c) between 21 keV, and 43 keV in reflection, and (d) between 43 keV and 60 keV in reflection.
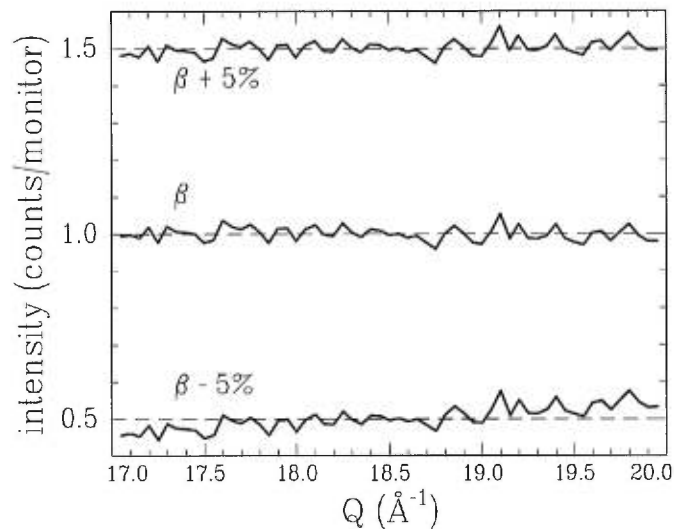
Figure 5. The amorphous silicon intensity ratio in the overlap region, between 21 keV and 43 keV, for different polarization correction constant: for β=93 % used during the correction, for a 5% larger β value offset by + 0.5, and for a 5% smaller value of β offset by -0.5.
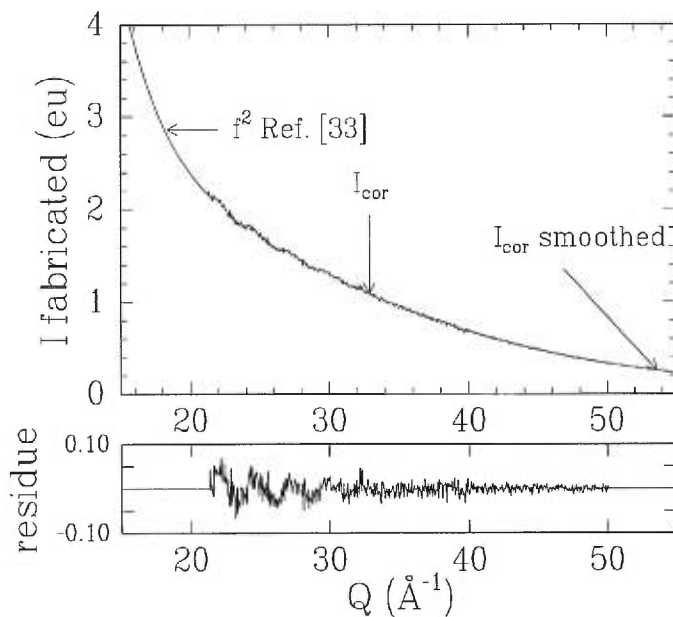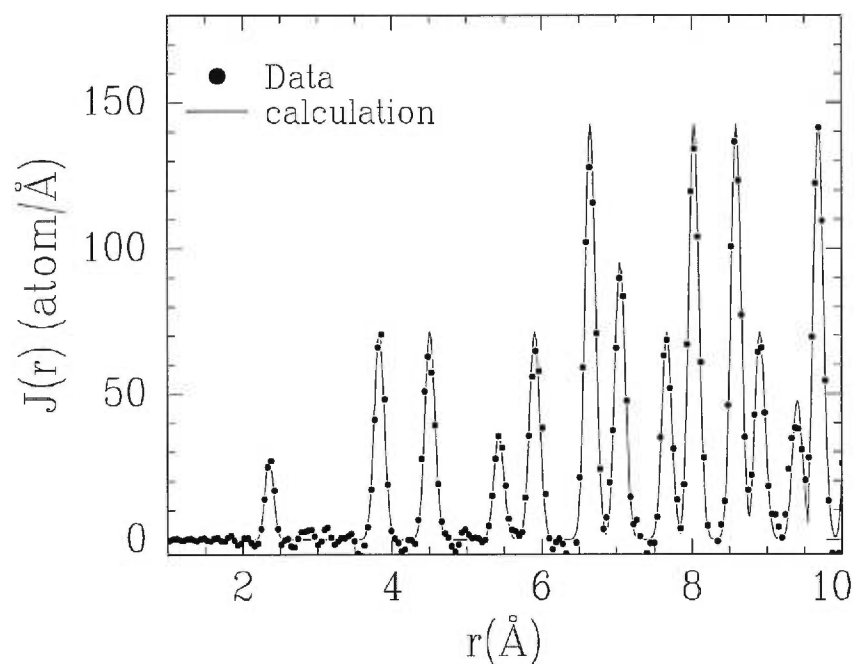

**Figure 6**. The intensity constructed to fit the extended region of f_{Si}^2. The residue is also shown.
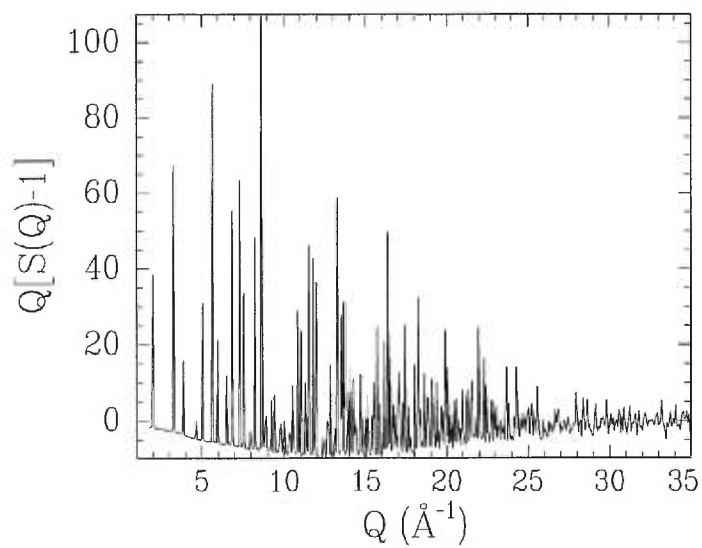
Figure 7. The interference function of powder c-Si determined by X-ray diffraction.
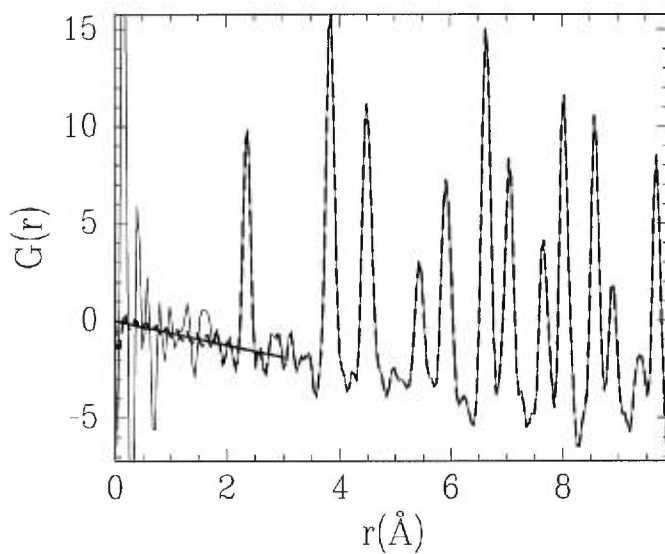
Figure 8. The reduced radial distribution function, *G(r)*, of powder c-Si sample before (----), and after (———) the Kaplow correction.

Figure 9. The radial distribution function, *J(r)*, of powdered crystalline silicon (dots). The solid line represents a theoretical calculation of the crystalline *J(r)* broadened by a Gaussian distribution.
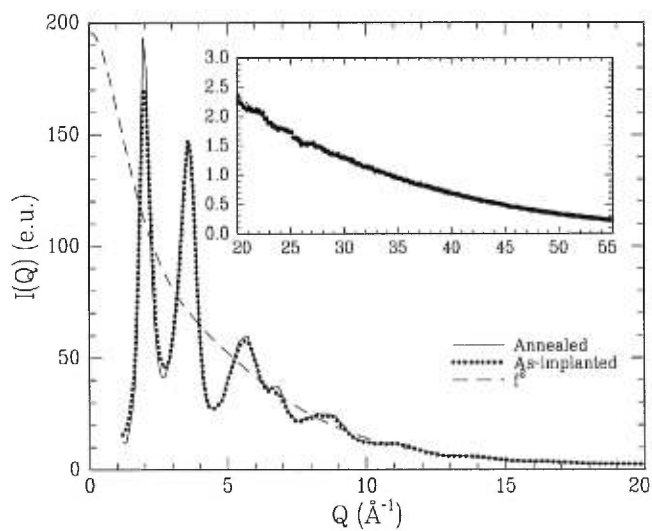
Figure 10. The normalized intensity in e.u., *I(Q)*, of the as-implanted (dotted line) and annealed (solid) amorphous silicon membranes, overlaid on f_{Si}^2 (dashed). The inset plot represents the extension of the plot to large *Q*.
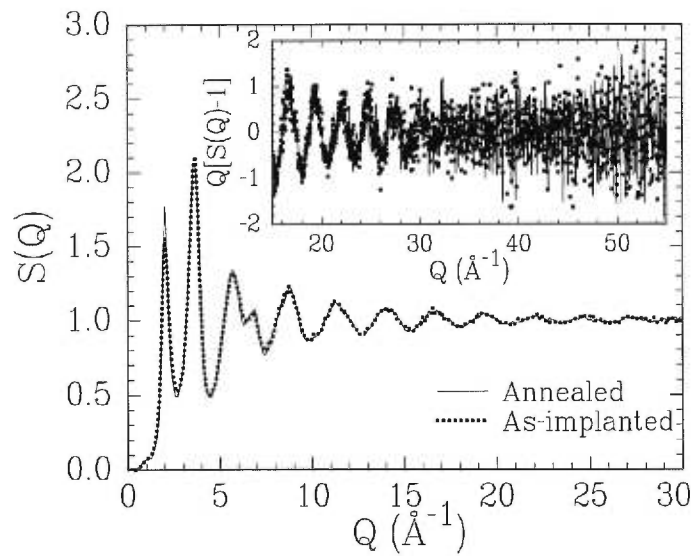
Figure 11. The structure factor, $S(Q)$, of the as-implanted (dashed) and annealed (solid) amorphous silicon membranes. The inset plot represents the corresponding interference functions, $F(Q)$, of the two samples in the high Q region.
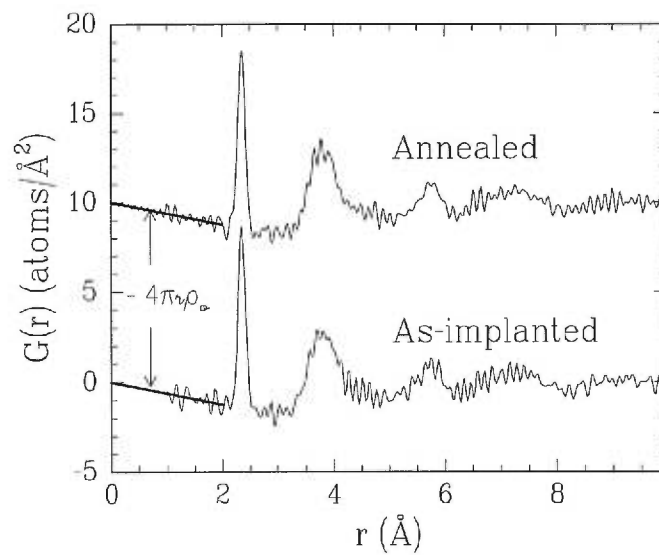
Figure 12. The reduced radial distribution function, $G(r)$, of annealed at 600°C (solid) and as-implanted (dotted line) a-Si. The straight line $-4\pi r \rho_o$ is also shown ($\rho_o = 0.049$ atom/Å^3).
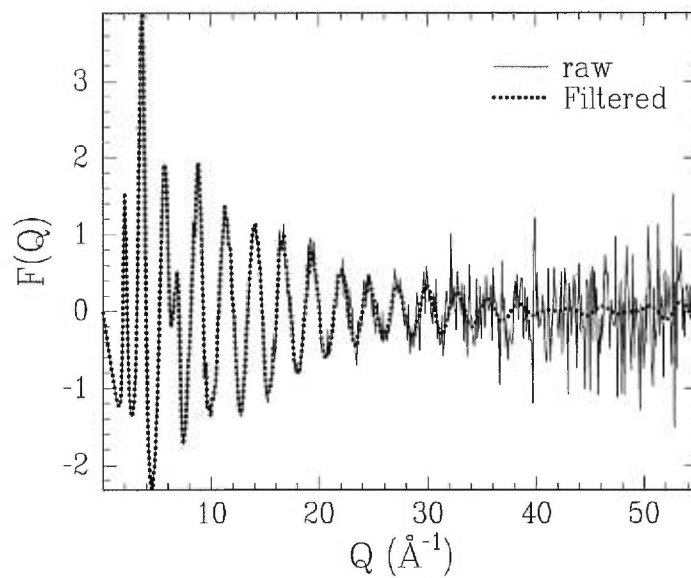
Figure 13. The interference functions of annealed a-Si , $F(Q)$, before (solid) and after (dotted line) filtering the noise at large Q.
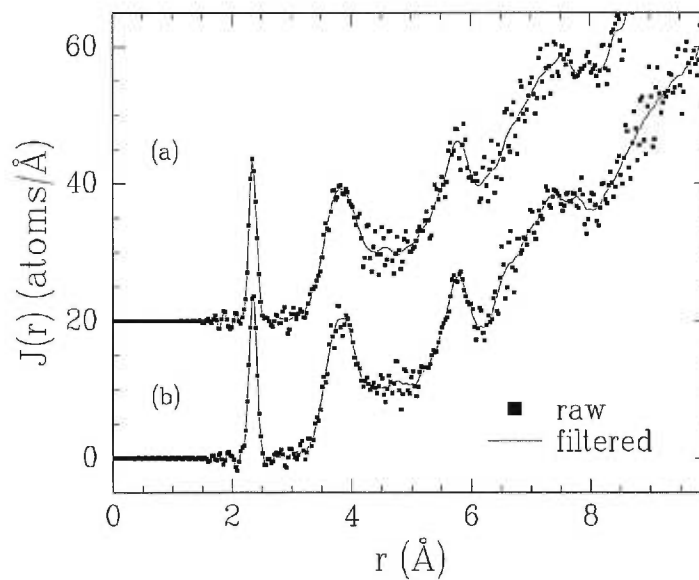
Figure 14. The RDF of the as-implanted (a) and annealed a-Si (b) sample calculated before (squares) and after (solid line) filtering the noise from $F(Q)$ at large Q as described in the text.
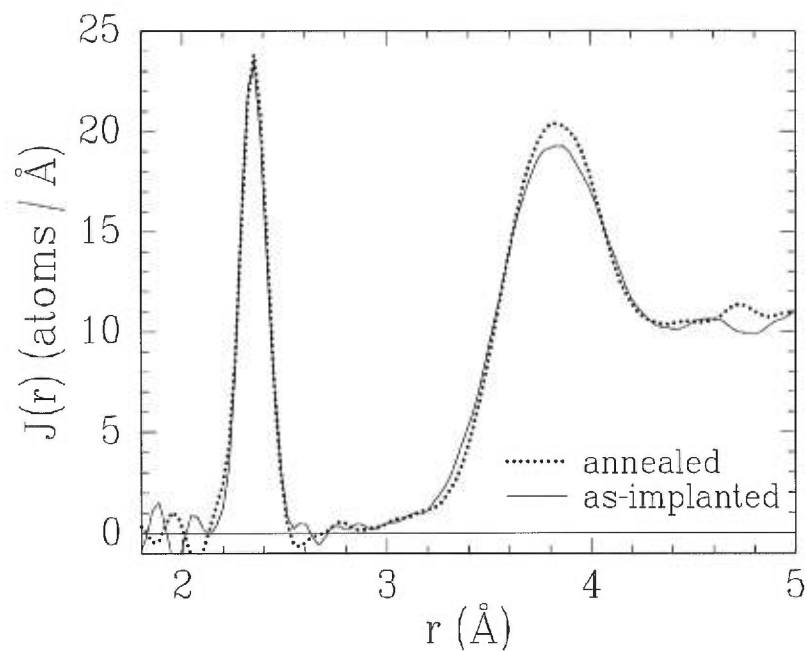
Figure 15. The radial distribution Function, *J(r),* of the annealed (solid line) and as-implanted (dashed line) a-Si membranes.
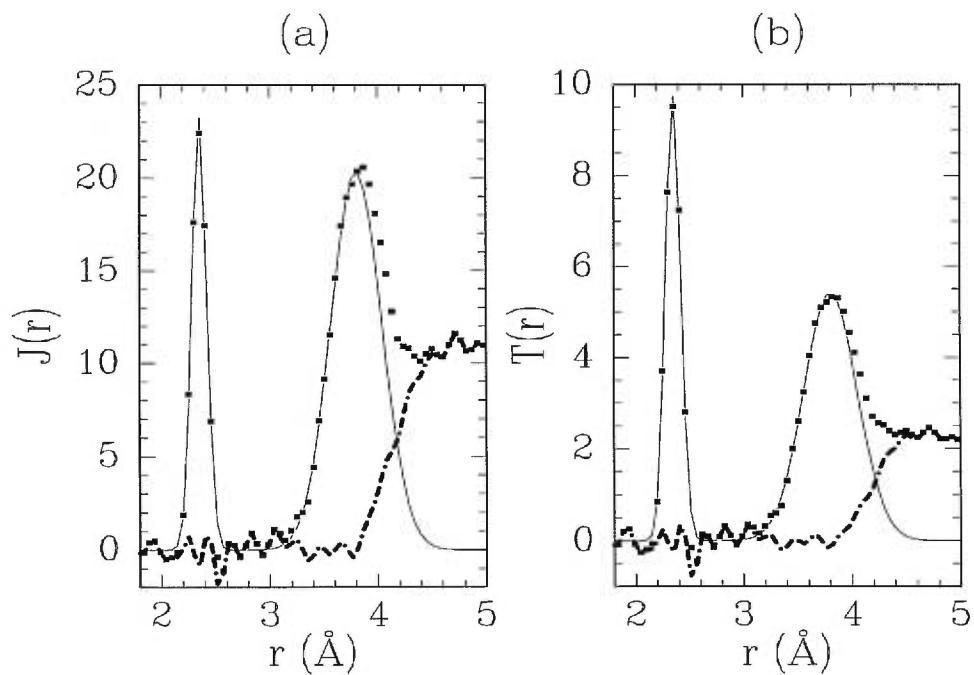
Figure 16. The Gaussian Fits (solid line) of the first and lower half of the second peaks of the function J(r) (square, a), and T(r) (square, b). The dotted-dashed curve is the residual fit.
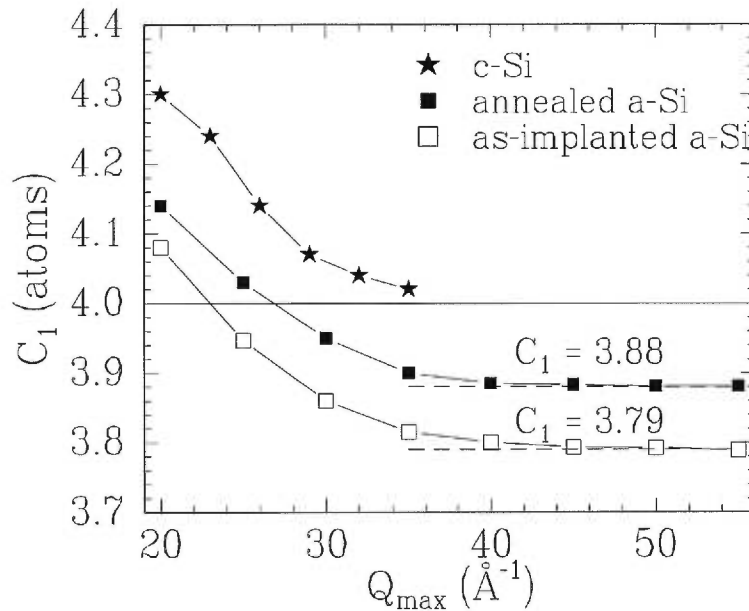
Figure 17. The coordination number of the first neighbor peak for the as-implanted (o) and annealed (v) a-Si, and that for the crystalline Si powder (H) as a function of Q_{max}.
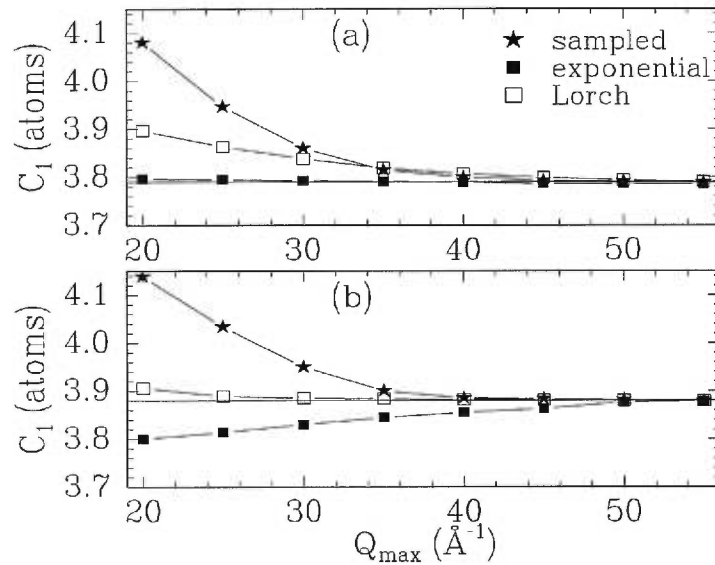
Figure 18. The coordination number of the first neighbor peak for the as-implanted (a) and annealed (b) a-Si, as deduced from J(r) determined via sampling (H), exponential damping (Eq. 21) (v), and Lorch damping (Eq. 20) (o) as a function of Q_{max}.

CONCLUSIONS

Nous avons présenté dans cette thèse des mesures de diffraction de rayons X ayant pour but de déterminer une fonction de distribution radiale précise et de haute résolution du silicium amorphe préparé par implantation ionique à haute énergie. Nous avons aussi déterminé, sous les mêmes conditions expérimentales, la fonction de distribution radiale d'une poudre de silicium cristallin qui a été utilisée comme mesure de référence.

La coordination du premier pic des fonctions de distribution radiale des échantillons du silicium amorphe et cristallin, déduit à partir de lissage de distribution gaussienne, a été déterminée de manière très précise. Nous avons trouvé que les coordinations des deux membranes du silicium amorphe sont respectivement de 3.79 ± 0.01 pour l'échantillon tel qu'implanté et de 3.88 ± 0.01 pour l'échantillon recuit, alors que la coordination de l'échantillon de poudre de Si-c est de 4.02 ± 0.05 atomes. L'incertitude sur les différents paramètres de structure (coordination et position atomique, désordre statique ..) est le fruit d'une analyse minutieuse des différentes sources d'erreurs qu'elles soient de natures expérimentale ou statistique. Nous avons aussi montré que pour obtenir des valeurs précises de la coordination, il faut couvrir une région de l'espace réciproque allant au moins jusqu'à $Q = 40$ Å^{-1} lors des mesures de diffraction; ceci en étudiant la variation de la coordination du premier pic, C_l, en fonction de Q_{max}. Nous avons observé un changement de coordination de l'ordre de

2% accompagné par des changements au niveau des pics correspondant aux plus grands voisins qui interviennent lors de la relaxation structurelle, ce qui nous laisse croire que la relaxation structurelle dans le silicium amorphe est due en grande partie à une annihilation mutuelle de défauts genre interstitiels et lacunes plutôt qu'à une réorganisation globale du réseau amorphe, ce qui serait très plausible vue que la densité de l'état relaxé et de celui tel qu'implanté est pareil. Le fait que la coordination C_I du Si-a est en deçà de 4 et que la distance entre premiers voisins change par 0.005 Å par rapport au cristallin, indiqueraient que le déficit de densité du Si-a par rapport au Si-c serait dû fondamentalement à une sous-coordination atomique. Cette dernière serait probablement due à la présence de défauts de genre lacunes dans la structure du silicium amorphe.

Les mesures de diffraction de rayons X ont couvert une très grande région de l'espace des Q (de 0.5 à 55 Å^{-1}); des mesures de diffusion de rayons X à faible angle réalisées antérieurement sur le même type de silicium amorphe ont été rajoutées aux mesures de diffraction pour couvrir une gamme de l'espace réciproque allant de 0.03 à 55 Å^{-1}. Lors des mesures de diffraction, une nouvelle méthode de lissage des spectres d'énergie collectés lors des mesures de diffractions a été développée. Nous avons démontré qu'en utilisant une fonction pic de nature asymétrique pour lisser le profil de diffusion élastique et des calculs de profils de diffusion *Compton*, basés sur la théorie dite «impulse approximation» pour lisser le pic inélastique (le programme permettant de générer un profil est décrit dans l'appendice), nous pouvons séparer de manière très efficace le pic de diffusion inélastique du pic de diffusion élastique et ce,

pour toute la gamme des mesures même pour celles correspondant à des angles de diffusion très petits (où les pics de diffusion cohérente et incohérente se chevauchent). Le facteur de diffusion atomique du silicium, f_{Si}, a été déterminé jusqu'à 55 Å^{-1}. Pour ce faire, nous avons développé une procédure itérative basée sur le fait que l'intensité de diffusion du silicium amorphe oscille autour du carré du facteur de diffusion atomique, $<f_{Si}^2>$. Finalement, une nouvelle approche pour filtrer les RDF du bruit statistique, inhérent aux mesures de diffraction dans la région des grandes valeurs de Q, a été développée.

Les membranes de silicium amorphe de 12 μm, préparées par implantation ionique et gravure chimique, utilisées lors des mesures de diffraction de rayons X sont de grande pureté puisqu'elles contiennent moins de 0.1 % atomique de contaminants tel que détecté par les mesures ERD-TOF (*Elastic Recoil Detection - Time Of Flight*). Nous avons démontré par des mesures de spectroscopie Raman sur les membranes amorphes que l'exposition aux rayons X de haute énergie n'induit pas de relaxation structurelle dans le Si-a. Ceci a été confirmé par les décalages dans les bandes TO (mode transverse optique) caractéristiques de chaque état (474 cm^{-1} pour l'échantillon tel qu'implanté et 483 cm^{-1} pour celui relaxé). L'absence d'impuretés, de densification et de dé-relaxation par les rayons X confirme que les changements observés dans les paramètres structuraux (coordination, position …) sont intrinsèques à la structure atomique du silicium amorphe.

APPENDICE

Ce programme permet de générer des profils de diffusion Compton en fonction de l'énergie pour une valeur de Q donnée. Le fichier d'entrée "Si_IA.dat" contient les paramètres nécessaire au calcul des profils [40]. Il faut par ailleurs ajouté une ligne juste après la première qui inclus les énergies de liaison des électrons dans chaque couche atomique tel qu'illusté dans l'exemple suivant:

K	1S	2S	2P	3S	3P	
↑	↑	↑	↑	↑	↑	
	2	2	6	2	2	← ELECTRONS_PAR_COUCHE
	1.839	0.1497	0.0998	0.00525	0.00112	← ENERGIE_LIAISON (AJOUTER)
0.00	6.35E-02	2.75E-01	1.49E-01	1.04E+00	7.44E-01	← DONNEE_IMPULSE_APPROX
0.05	6.35E-02	2.75E-01	1.49E-01	1.03E+00	7.44E-01	
0.10	6.35E-02	2.74E-01	1.49E-01	9.92E-01	7.43E-01	
0.15	6.35E-02	2.73E-01	1.49E-01	9.40E-01	7.39E-01	
0.20	6.35E-02	2.72E-01	1.49E-01	8.72E-01	7.28E-01	
0.30	6.34E-02	2.68E-01	1.49E-01	7.07E-01	6.81E-01	
0.40	6.33E-02	2.62E-01	1.49E-01	5.31E-01	5.97E-01	
0.50	6.32E-02	2.55E-01	1.49E-01	3.74E-01	4.90E-01	
0.60	6.31E-02	2.47E-01	1.48E-01	2.48E-01	3.80E-01	
0.70	6.30E-02	2.37E-01	1.48E-01	1.58E-01	2.81E-01	
0.80	6.28E-02	2.27E-01	1.47E-01	9.79E-02	2.01E-01	
1.00	6.24E-02	2.05E-01	1.45E-01	4.07E-02	9.46E-02	
1.20	6.19E-02	1.81E-01	1.42E-01	2.56E-02	4.19E-02	
1.40	6.14E-02	1.56E-01	1.37E-01	2.37E-02	1.83E-02	
1.60	6.08E-02	1.32E-01	1.31E-01	2.35E-02	8.72E-03	
1.80	6.01E-02	1.10E-01	1.24E-01	2.21E-02	5.24E-03	
2.00	5.93E-02	9.06E-02	1.16E-01	1.94E-02	4.21E-03	
2.40	5.76E-02	5.84E-02	9.92E-02	1.29E-02	4.01E-03	
3.00	5.45E-02	2.79E-02	7.40E-02	5.66E-03	3.60E-03	
4.00	4.88E-02	8.22E-03	4.14E-02	1.16E-03	2.17E-03	
5.00	4.25E-02	4.50E-03	2.21E-02	3.61E-04	1.15E-03	
6.00	3.63E-02	4.25E-03	1.18E-02	2.87E-04	5.99E-04	
7.00	3.04E-02	4.12E-03	6.36E-03	2.83E-04	3.19E-04	
8.00	2.52E-02	3.69E-03	3.52E-03	2.58E-04	1.74E-04	
10.00	1.7E-02	2.5E-03	1.2E-03	1.8E-04	5.69E-05	
15.00	5.6E-03	7.0E-04	1.1E-04	4.9E-05	5.2E-06	
20.00	2.0E-03	2.1E-04	1.7E-05	1.4E-05	7.7E-07	
30.00	3.2E-04	2.8E-05	9.4E-07	1.9E-06	4.3E-08	
40.00	7.3E-05	5.9E-06	1.1E-07	3.9E-07	5.0E-09	
60.00	7.8E-06	5.9E-07	4.9E-09	3.9E-08	2.2E-10	

```c
#include <stdio.h>
#include <stdlib.h>
#include <string.h>
#include <math.h>
// Entrée des paramètres de calibration
//-------------------------------------------------------------------
#define NUM_CANAL          1024   // Nombre de canaux MCA
#define ENERGIE_PAR_CANAL 0.02   // Énergie par canal (keV/canal)
#define ENERGIE_CANAL_0   0.33   // Énergie du canal 0 (keV)
#define FWHM_ELASTIC        14     // Largeur à mi-hauteur du pic élastique
//-------------------------------------------------------------------


// Définition des autres constantes du programme
#define ENERGIE_INCIDENTE       13     // Énergie incidente (keV)
#define FRACTION_NON_POLARISE  0.02   // Fraction de rayons X non polarisée
#define NUM_K              31     // Paramètre interne de l'IA
#define NUM_COUCHE              5      // Nombre de couches atomiques
//-------------------------------------------------------------------
// Initialiser la fonction permettant de convertir Q en 2θ
double CALCULER_2THETA (double q);
double IMPULSE_APPROX (double E, double tth);


// Programme principal
void main (void)
{
double 2THETA, Q, somme, COMPTON[NUM_CANAL+1], COMPTON_CONV[NUM_CANAL+1],
       CONVOLUE[NUM_CANAL+1],ENERGIE[NUM_CANAL+1],ENERGIE_LIAISON[10],
       K[50],DONNEE_IMPULSE_APPROX[50][10], ELECTRONS_PAR_COUCHE [10];
FILE   *donnee_impulse, *donnee_Compton;
char   record[255];
int    i,j;
donnee_impulse=fopen("Si_IA.dat"."r");
while (!feof(donnee_impulse)) {
fgets (record,sizeofrecord, donnee_impulse);
sscanf (record, "%lf %lf %lf %lf %lf",
       & ELECTRONS_PAR_COUCHE[0], & ELECTRONS_PAR_COUCHE[1],
       & ELECTRONS_PAR_COUCHE[2], & ELECTRONS_PAR_COUCHE[3],
       & ELECTRONS_PAR_COUCHE[4]);
fgets (record,sizeofrecord, donnee_impulse);
sscanf (record, "%lf %lf %lf %lf %lf",
```

```
        & ENERGIE_LIAISON [0], & ENERGIE_LIAISON [1],
        & ENERGIE_LIAISON [2], & ENERGIE_LIAISON [3],
        & ENERGIE_LIAISON [4]);
for (i=0; i < NUM_K; i++) {
fgets (record,sizeofrecord, donnee_impulse);
sscanf (record, "%lf %lf %lf %lf %lf", &K[i]
        & DONNEE_IMPULSE_APPROX [i][0], & DONNEE_IMPULSE_APPROX [i][1],
        & DONNEE_IMPULSE_APPROX [i][2], & DONNEE_IMPULSE_APPROX [i][3],
        & DONNEE_IMPULSE_APPROX [i][4]);
}
} fclose (donnee_impulse);


Donnee_Compton=fopen("Si_compton.dat","w");
// Calcul du profil de compton pour une valeur de Q de 5Å⁻¹
2THETA= CALCULER_2THETA (5);
// Calculer les valeurs du vecteur énergie
for (i=0; i < NUM_CANAL+1; i++)
        ENERGIE[i]= ENERGIE_CANAL_0 + (i*ENERGIE_PAR_CANAL);
// Initialiser toute les variables compton à 0
for (i=0; i < NUM_CANAL+1; i++) {
        COMPTON[i]=0.0;
        COMPTON_CONV[i]=0.0;
}
// Calculer les valeurs du vecteur Compton
for (i=25; i < NUM_CANAL-25; i++) {
        COMPTON[i]= (0.25*ENERGIE_PAR_CANAL)*(
        (0.5* IMPULSE_APPROX( ENERGIE[i]-(0.5*ENERGIE_PAR_CANAL), 2THETA)) +
        IMPULSE_APPROX( ENERGIE[i]-(0.25*ENERGIE_PAR_CANAL), 2THETA) +
        IMPULSE_APPROX( ENERGIE[i], 2THETA) +
        IMPULSE_APPROX( ENERGIE[i]+(0.25*ENERGIE_PAR_CANAL), 2THETA) +
        (0.5* IMPULSE_APPROX( ENERGIE[i]+(0.5*ENERGIE_PAR_CANAL), 2THETA)));
}
somme=0.0;
for (i=0; i < 41; i++) {
CONVOLUE[i]=0.25* FWHM_ELASTIC*sqrt(PI/log(2.0))*(
            erf(2*sqrt(log(2.0))/ FWHM_ELASTIC*((i-20)+0.5)) +
            erf(2*sqrt(log(2.0))/ FWHM_ELASTIC*((20-i)+0.5)));
somme += CONVOLUE[i];
}
for (i=0; i < 41; i++)
        CONVOLUE[i] = CONVOLUE[i] / somme;
```

```
for (i=25; i < NUM_CANAL-25; i++) {
COMPTON_CONV[i] = 0.0;
        for (j=0; j < 41; j++)
        COMPTON_CONV[i] = COMPTON[i+(j-20)]* CONVOLUE[i];
}
for (i=0; i < NUM_CANAL+1; i++) {
fprintf(Donnee_Compton, "%9.4f  %16.8f\n",ENERGIE[i], COMPTON_CONV[i]);
fclose(Donnee_Compton);
}
}
//Fonction permettant de déduire l'angle 2θ correspondant à une valeur de Q
double CALCULER_2THETA (double q)
{
return 2*asin(q*0.98664/ ENERGIE_INCIDENTE);
}
// Fonction retournant une valeur du Compton associé à une énergie et un
angle 2θ
double IMPULSE_APPROX (double E, double tth)
{
double cos_angle, momentum_trans, proj_momentum,
        delata_K, delta_K_proj, f1, f2, x, comp;
int    i, j, indice;
if (E > ENERGIE_INCIDENTE)
        return 0.0;
cos_angle = cos(tth);
momentum_trans = sqrt (ENERGIE_INCIDENTE* ENERGIE_INCIDENTE) + (E*E) -
                        (2.0*ENERGIE_INCIDENTE*E*cos_angle));
proj_momentum = (ENERGIE_INCIDENTE*E*(1-cos_angle)) -
                (511.0*(ENERGIE_INCIDENTE-1));
proj_momentum *=  137.0 / (511.0 * momentum_trans);
proj_momentum = fabs(proj_momentum);
comp = 0.0, indice = -1;
for (i = 0; i < NUM_K; i++)
if (proj_momentum < K[i]) {
indice = i;
break;
}
if (indice < 0) {
indice = NUM_K-1;
f1 = 0.0;
```

```
f2 = 1.0;
delta_K = 0.0;
delta_K_proj = 0.0;
}
else {
delta_K = K[indice] - K[indice-1];
delta_K_proj = proj_momentum - K[indice-1];
f2 = delta_K_proj / delta_K;
f1 = 1.0 - f2;
}
comp = 0.0;
for (i = 0; i < NUM_COUCHE; i++)
if ((ENERGIE_INCIDENTE-E) > ENERGIE_LIAISON [i])
comp += ENERGIE_LIAISON[i] * (f1*DONNEE_IMPULSE_APPROX[indice-1][i]) *
        (f2*DONNEE_IMPULSE_APPROX[indice][i]);
comp *= 121.72 * (ENERGIE_INCIDENTE / E) / momentum_trans;
comp*=1.0 - FRACTION_NON_POLARISE+
        (FRACTION_NON_POLARISE*cos_angle*cos_angle);
comp *= (E*E) / (ENERGIE_INCIDENTE *ENERGIE_INCIDENTE);
return comp;
}
```

BIBLIOGRAPHIE

[1] B. E. Warren, *X-Ray Diffraction*, Addisson-Wesley, Reading Mass. (1969).

[2] S.R. Elliott, *Physics of amorphous materials*, Longman Inc., NY. (1990).

[3] R. Zallen, *The Physics of amorphous materials*, John Wiley & Sons (1983).

[4] W. H. Zachariasen, J. Am. Chem. Soc. **54**, 3841 (1932).

[5] S.C. Moss et J.F. Graczyk, Phys. Rev. Lett. **23**, 1167 (1969).

[6] D. E. Polk, J. Non-Cryst. Solids **5**, 365 (1971).

[7] D. E. Polk and D. S. Boudreaux, Phys. Rev. Lett. **31**, 92 (1973).

[8] G. A. N. Connell et R. J. temkin, Phys. Rev. B **9**, 5323 (1974).

[9] L. Guttman, Phys. Rev. B **64**, 1866(1974).

[10] F. Wooten, K. Winer et D. Weaire, Phys. Rev. Lett. **54**, 1392 (1985).

[11] R. Car et M. Parrinello, Phys. Rev. Lett. **60**, 204 (1988).

[12] W. D. Luedtke et U. Landman, Phys. Rev. B **40**, 1164 (1989).

[13] I. Stich, R. Car et M. Parrinello, Phys. Rev. B **44**, 11092 (1991).

[14] M. Ishimaru, S. Munetoh et T. Motooka, Phys. Rev. B **56**, 15133 (1997).

[15] N. Mousseau et L. J. Lewis, Phys. Rev. Lett. **78**, 1484 (1997).

[16] S.C. Moss et J.F. Graczyk, Proc. 10th Int. Conf. Phys. Semicond., ed. S. Keller (Cambridge MA, 1970).

[17] R. Mosseri, C. Sella et J. Dixmier, Phys. Stat. Sol. (a) **52**, 475 (1979).

[18] A. Menelle, A.M. Flank, P. Lagarde et R. Bellissent, J. de Phys. **C8**, suppl. au **12**, 379 (1986).

[19] J. Fortner et J.S. Lannin, Phys. Rev. **B39**, 5527 (1989).

[20] J. Fortner et J.S. Lannin, J. Non-Cryst. Solids **106**, 128 (1988).

[21] A. Filipponi, F. Evangelisti, M. Benfatto, S. Mobilio et C.R. Natoli, Phys. Rev. **B40**, 9636 (1989).

[22] S. Kugler, G. Molnár, G. Petö, E. Zsoldos, L. Rosta, A Menelle et R. Bellissent, Phys. Rev. B **48**, 7685 (1993).

[23] S. Kugler, L. Pusztai, L. Rosta, P. Chieux and R. Bellisent, Phys. Rev. B **48**, 8030 (1993) .

[24] R.J. Temkin, W. Paul et G.A.N. Connell, Adv. in Phys. **22**, 581 (1973).

[25] I. Ohdomari, M. Kakumu, H. Sugahara, M. Mori, T. Saito, T. Yonehara et Y. Hajimoto, J. Appl. Phys. **52**, 6617 (1981).

[26] D. L. Williamson, S. Roorda, M. Chicoine, R. Tabti, P. A. Stock, S. Acco et F. W. Saris, Appl. Phys. Lett. **67**, 226 (1995).

[27] J. Mayer, L. Eriksson et J. A. Davies, *Ion implantation in semiconductors*, Academic Press (1970).

[28] J. M. Poate et J. S. Williams, *Ion implantation and ion beam processing*, Academic Press (1984).

[29] J. F. Ziegler , *Ion implantation science and technology*, Academic Press (1984).

[30] S. T. Picraux et P. S. Peercy, *Ion implantation of surfaces*, Scientific American, Mars, (1985).

[31] G. L. Olsen et J. Roth, *Mater. Sc. Rep.*, **3** (1989).

[32] J. S. Custer, M. O. Thomson, D. C. Jacobson, J. M. Poate, S. Roorda, W. C. Sinke et F. Spaepen, Appl. Phys. Lett. **64**, 437 (1994).

[33] K. Laaziri, S. Roorda et J.-M. Baribeau, J. Non-Cryst. Solids **191**, 193 (1995).

[34] S. Roorda, S. Doorn, W. C. Sinke, P. M. L. O. Scholte et E. van Loenen, Phys. Rev. Lett. **62**, 1880 (1989).

[35] R. Tsu, J.G. Hernandez, and F.H. Pollak, Solid State Communication, **54**, 447 (1985).

[36] S. Roorda, W. C. Sinke, J. M. Poate, D. C. Jacobson, S. Dierker, B. S Denis, D. J. Eagelsham, F. Spaepen et P. Fuoss, Phys. Rev. B **44**, 3702 (1991).

[37] S. Roorda, J. M. Poate et D. C. Jacobson, Appl. Phys. Lett. **55**, 1516 (1989).

[38] S. Coffa, J. M. Poate, D. C. Jacobson, W. Frank et W. Gustin, Phys. Rev. B **45**, 8355 (1992).

[39] A. Battaglia, S. Coffa, F. Priolo, G. Compagnini et G. A. Baratta, Appl. Phys. Lett. **63**, 2204 (1993).

[40] F. Biggs, L. B. Mendehlson et J.B. Mann, Atomic Data and Nuclear Data Tables **16**, 201 (1975).

CONTRIBUTION DE L'AUTEUR

Article 1: **Edge supported amorphous silicon membranes for diffraction studies.**

Nucl. Instrum. & Meth. B **148**, 360 (1999)

Auteurs: Sjoerd Roorda, **Khalid Laaziri,** and Subhash C. Gujrathi.

J'ai préparé les membranes de silicium amorphe (implantation et attaque chimique) présentées dans cet article. Lors du développement de la méthode de préparation, j'ai supervisé des étudiants d'été (R. Tabti, M. Chicoine, F. Tessier et R. Poirier). J'ai assisté le professeur Subhash Gujrathi lors des mesures de détection par recul élastique (ERD). Les mesures Raman ont été effectuées par mon directeur Sjoerd Roorda, il a aussi eu l'initiative d'écrire cet article pour la conférence d'IBMM98 (Ion Beam Modification of Materials, Amsterdam 1998).

Article 2: **Quantitative treatment for extracting coherent elastic scattering from X-ray scattering experiments**

J. of Appl. Cryst. **32**, 322 (1999)

Auteurs: Khalid Laaziri, J. L. Robertson, S. Roorda, M. Chicoine, S. Kycia, J. Wang, and S. C. Moss.

J'ai eu l'idée d'utiliser les calculs théoriques de profil de Compton pour lisser les spectres de diffusion totale. J'ai modifié un programme écrit par Lee Robertson afin de l'adapter à nos besoins. J'ai eu aussi l'idée d'utiliser des fonctions analytiques de type asymétriques pour lisser les pics de diffusion élastique. Toutes les mesures expérimentales présentées dans cet article ont été réalisées avec l'aide de mes collaborateurs. J'ai participé à l'élaboration des idées, mis en place toute les procédures et effectué tous les calculs. En tant que premier auteur, j'ai été responsable de la rédaction de l'article.

Article 3: **High Energy X-Ray Diffraction Study of Pure Amorphous Silicon**

Auteurs: Khalid Laaziri, S. Kycia, S. Roorda, M. Chicoine, J. L. Robertson, J. Wang, and S. C. Moss.

Article 4: **High Resolution Radial Distribution Function of Pure Amorphous Silicon**

Physical Review Letters **82**, 3460 (1999).

Auteurs:Khalid Laaziri, S. Kycia, S. Roorda, M. Chicoine, J. L. Robertson, J. Wang, and S. C. Moss.

J'ai participé à la mise en place du dispositif expérimental, ainsi qu'à la prise de données. Toutes les mesures expérimentales présentées dans cet travail ont été réalisées avec l'aide de mes collaborateurs, plus particulièrement Stefan Kycia, Martin Chicoine et mon directeur Sjoerd Roorda. J'ai eu l'idée d'utiliser de nouvelles procédures de filtrage des transformées de Fourier, ainsi que la détermination du facteur de diffusion atomique, f, dans les grandes régions de l'espace des Q. J'ai effectué les calculs et j'ai participé à l'élaboration des conclusions tirées de l'analyse des résultats. En tant que premier auteur, j'ai été responsable de la rédaction des deux articles 3 et 4.

REMERCIEMENTS

Je suis énormément reconnaissant envers mon directeur de recherche, Sjoerd Roorda, pour m'avoir fourni cet encadrement professionnel, exigeant mais Ô combien stimulant, qui a permis, j'en suis convaincu, de mener à bon terme ce travail. Plus qu'une source de précieux et judicieux conseils, Sjoerd a su développer mon expérience de la physique et enrichir ma passion pour cette science.

Merci énormément aussi à mes collaborateurs dans ce projet, Stefan Kycia, Martin Chicoine, Lee Robertson et Simon Moss, avec qui ce fut un plaisir de collaborer. Ce travail ne saurait être ce qu'il est devenu n'eut été des nombreuses discussions scientifiques fructueuses que nous avons eu tous ensemble. Je me rappellerai à toujours mes séjours au laboratoire CHESS à l'université Cornell, surtout des longues nuits blanches à mettre en place le dispositif expérimental et à récolter les données. Au delà de la souffrance mentale et physique que nous avons subie avec Stefan et Martin, nous avons réussi à créer une solide amitié et à passer d'excellents moments, je tiens de nouveau à vous remercier de tout cœur.

J'aimerais remercier Laurent Lewis pour son appui et pour ses conseils éclairés, ainsi que les membres du Groupe de recherche en physique et technologie des couches minces (GCM) notamment Mourad, Ghyslain qui ont été de précieux supports. Un grand merci au personnel du laboratoire René J-A Lévesque, particulièrement Hélène Lamothe pour les mille et un services rendus et les experts des accélérateurs Pierre Bérichon et Réal Gosselin.

Je voudrais finalement adresser un merci tout spécial : À ma belle famille, particulièrement elhaj, elhajja, merci pour vos prières. À mes proches notamment mon oncle Ahmed, sa femme ainsi que ses enfants Nabil, Hind et Anas. À mes amis(es), spécialement Souad et Chouhaid. À tout le monde, merci d'avoir partagé avec moi durant toutes ces années la joie des bons moments, le sérieux des moments plus difficiles et le comique des moments franchement insupportables, ils ont incontestablement contribué à l'aboutissement de ce travail chacun à sa façon.